The role of integral gain and its neuromuscular implementation in the flight control system of *Drosophila melanogaster*

Thesis by

Francesca V. Ponce

In Partial Fulfillment of the Requirements for the
degree of
Doctor of Philosophy

Caltech

CALIFORNIA INSTITUTE OF TECHNOLOGY
Pasadena, California

2024
Defended May 30, 2024

Francesca V. Ponce
ORCID: 0000-0002-9070-2780

ACKNOWLEDGEMENTS

I am deeply grateful to my family, friends, and mentors whose support have made the following work possible. My time as a graduate student has been filled with great friendships and memories I will cherish forever. Thank you to everybody that has been part of my community during these years.

I would like to acknowledge my advisor, Michael Dickinson, thank you for your scientific guidance through the high and lows of my journey at Caltech. Your reliable and honest feedback during all these years have made this work possible and have shaped me as scientist. Thank you for sharing your knowledge about flies, tick marks, and steering muscles during our many chats. I would also like to thank my committee members, Betty Hong, Joe Parker, and Thanos Siapas, for your helpful feedback and encouragement.

As a grad student in the Dickinson lab, I have been lucky to get support from many mentors and friends. Special thanks to Kate Leitch for organizing the memorable trips to Coyote Lake, and for being a wonderful friend I can always count on. To Román Corfas, thank you for your always thoughtful advice, encouragement, and for being a fantastic friend during all these years. To Will Dickson, thank you for teaching me with great patience all I know about PI controllers. I would also like to thank Ivo Ros, Jaison Omoto, Thad Lindsey, Johan Melis, Ysabel Giraldo, Sam Whitehead, and Floris van Breugel, for their scientific advice and support.

My time in Pasadena would not have been the same without the friendship of Khan Manther, Peishi Cheng, Kellan Morse, Kriti Sharma, Tarun Sharma, Aaron Schneeberger, Nataly Evans, Kavi Rangan, and Donovan Ventimiglia, thank you for all the chats, and fun times shared. I would also like to acknowledge all the members of Socialists of Caltech and the Pasadena Tenants Union, I am deeply grateful to all of you, and feel so lucky to have learned and organized with such a special community.

To my parents, Varsovia Cevallos and Patricio Ponce, thank you for love, and unwavering support. Your scientific curiosity inspired me to start graduate school, and your love and incessant encouragement have kept me going. Thank you for always being the source of sound advice I can count on. To my late grandmother, thank you for your love and teachings, and thank you to my siblings, Joan, Amanda, and Leandro, for all the support, memes, and dog pics you share with me.

ABSTRACT

Small flying insects such as the fruit fly, *Drosophila melanogaster*, can navigate along a relatively straight path for long distances. During these journeys they need a long-range navigational strategy to maintain a constant heading over time, as well as stabilizing behaviors to deal with perturbations, such as a sudden gust of wind, or a broken wing. In this work, I characterize behavioral strategies flies use to maintain stable flight using a combination of experimental and control theoretic approaches. I then investigate how this control strategy is implemented in the flight motor system. In Chapter 1, I describe release-and-recapture experiments performed in the Mojave Desert to investigate how flies interact with the wind to travel long distances. These experiments provide key insight into the dispersal behavior of small insects and suggest that these animals employ a single algorithm that is functionally robust in both still air and under windy conditions. In Chapter 2, I present an extensive set of behavioral experiments showing that the optomotor response, a well-described stabilizing flight reflex, can be accurately modelled by a proportional-integral controller. I also show simulations that exemplify the potential functional advantage of this controller model in natural flight conditions. In Chapter 3, I performed muscle imaging experiments to investigate how the integral gain of a proportional integral controller might be implemented within the flight motor system. Finally, in Chapter 4, I summarize the main findings, and discuss limitations of this work and future directions.

PUBLISHED CONTENT AND CONTRIBUTIONS

Leitch, K. J., Ponce, F. V., Dickson, W. B., van Breugel, F. and Dickinson, M. H. (2021). The long-distance flight behavior of *Drosophila* supports an agent-based model for wind-assisted dispersal in insects. *Proceedings of the National Academy of Sciences* 118, e2013342118. doi: https://doi.org/10.1073/pnas.2013342118

Author contributions: K.J.L., F.v.B., and M.H.D. designed research; K.J.L., F.V.P., F.v.B., and M.H.D. performed research; W.B.D. contributed new reagents/analytic tools; K.J.L. and W.B.D. analyzed data; and K.J.L., W.B.D., and M.H.D. wrote the paper.

TABLE OF CONTENTS

LIST OF ILLUSTRATIONS AND/OR TABLES

Number *Page*

LIST OF TABLES

Number *Page*

Chapter 1

THE LONG-DISTANCE FLIGHT BEHAVIOR OF *DROSOPHILA* SUPPORTS AN AGENT-BASED MODEL FOR WIND-ASSISTED DISPERSAL IN INSECTS

Leitch, K. J., Ponce, F. V., Dickson, W. B., van Breugel, F. and Dickinson, M. H. (2021). The long-distance flight behavior of *Drosophila* supports an agent-based model for wind-assisted dispersal in insects. *Proceedings of the National Academy of Sciences* 118, e2013342118. doi: https://doi.org/10.1073/pnas.2013342118

Author contributions: K.J.L., F.v.B., and M.H.D. designed research; K.J.L., F.V.P., F.v.B., and M.H.D. performed research; W.B.D. contributed new reagents/analytic tools; K.J.L. and W.B.D. analyzed data; and K.J.L., W.B.D., and M.H.D. wrote the paper.

1.1 Abstract

Despite the ecological importance of long-distance dispersal in insects, its mechanistic basis is poorly understood in genetic model species, in which advanced molecular tools are readily available. One critical question is how insects interact with the wind to detect attractive odor plumes and increase their travel distance as they disperse. To gain insight into dispersal, we conducted release-and-recapture experiments in the Mojave Desert using the fruit fly, *Drosophila melanogaster*. We deployed chemically baited traps in a 1 km radius ring around the release site, equipped with cameras that captured the arrival times of flies as they landed. In each experiment, we released between 30,000 and 200,000 flies. By repeating the experiments under a variety of conditions, we were able to quantify the influence of wind on flies' dispersal behavior. Our results confirm that even tiny fruit flies could disperse ∼12 km in a single flight in still air and might travel many times that distance in a moderate wind. The dispersal behavior of the flies is well explained by an agent-based model in which

animals maintain a fixed body orientation relative to celestial cues, actively regulate groundspeed along their body axis, and allow the wind to advect them sideways. The model accounts for the observation that flies actively fan out in all directions in still air but are increasingly advected downwind as winds intensify. Our results suggest that dispersing insects may strike a balance between the need to cover large distances while still maintaining the chance of intercepting odor plumes from upwind sources.

1.2 Introduction

Insects from diverse taxa, such as butterflies, locusts, and dragonflies, undertake seasonal mass migrations traveling up to thousands of kilometers to their destination as a strategy to survive a seasonally changing environment (Merlin et al., 2012). In contrast to other taxonomic groups of migratory animals, such as birds and mammals, that typically perform round-trip migrations and repeat multiple trips during their lifetime, insects exhibit a great diversity of spatiotemporal migration strategies. For example, monarch butterflies perform round-trip migrations, while mustard aphids engage in seasonal mass movements radiating from a source site (Drake and Gatehouse, 1995), but do not return to the same location. In addition to seasonal migratory insects, many smaller insects engage in non-cyclic long distance dispersal behaviors. While insects are the most abundant class of terrestrial migrants, with trillions of insects moving across the globe, their navigational strategies have only recently become a focus of study due to advancements in tracking technology (Chapman et al., 2011).

The dispersal of small insects across landscapes has often modeled using stochastic processes such as diffusion and advection, which tend to underestimate the insects' ability to actively maintain stable trajectories over large distances. However, mark-recapture experiments conducted decades ago in Death Valley (Coyne et al., 1982; Jones et al., 1981) showed that flies can travel several kilometers in a single evening (Figure 1.1). These experiments aimed to determine whether flies could disperse among isolated populations, potentially explaining the genetic similarities observed between geographically isolated fly populations. Specifically, the release and recapture experiment tested the ability of flies to disperse long distances between habitable oases separated by resource-poor landscapes. Given the limited opportunities for refueling, and knowing the energetic limits of these flies, their travel distances suggest that flies likely held a relatively straight trajectory during flight (Dickinson, 2014). While these experiments showed flies can travel long distances maintaining a straight trajectory, the navigational strategies they use were unclear. More recently, the Dickinson lab performed similar release-and-recapture experiments in the Mojave Desert using the fruit fly, *Drosophila melanogaster*, to better understand how small insects can travel in a relatively straight path despite environmental variables like wind (Leitch et al., 2021).

Although the previous studies showed flies can disperse over long distances, they left open several critical questions. First, it was not clear whether individual flies dispersed in random directions or whether the population movement was biased by external conditions, such as the wind, geographical features, or celestial cues. Second, because the precise transit times of the flies were not known, it was impossible to estimate the actual groundspeeds used by the animals as they dispersed. To provide more clarity to these and other questions related to long-distance dispersal, we conducted a series of release-and-recapture experiments in the Mojave Desert. We equipped circular arrays of chemically baited traps with simple machine vision systems that captured the arrival times of flies as they landed and repeated the experiments under a variety of ambient wind conditions. The results provide key insight into the behavioral algorithms used by *Drosophila* while dispersing in the wild and serve as the basis for a general agent-based model of wind-assisted dispersal in insects.

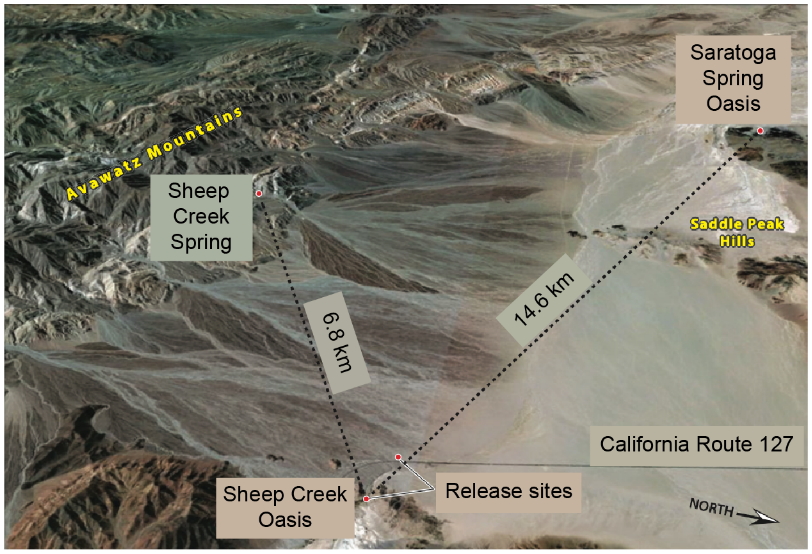

Figure 1.1: Google earth photo of the area in Death Valley where the 1981 mark-and-recapture experiments were performed.

Flies were released from two release sites approximately 1 km apart. Flies from both release sites made it to the oases at Saratoga Spring and Sheep Creek Spring. Figure reproduced from (Dickinson, 2014).

Insects use celestial cues to navigate

Without external reference, any animal, will very quickly walk in circles (Cheung et al., 2007), thus insects engaging in long-distance displacement require some form of navigation to maintain a constant heading over time to complete these journeys. For example, monarch butterflies (*Danaus plexippus*), which travel every autumn from North America to overwintering locations in Central Mexico (Reppert and Roode, 2018), rely on the sun as their main orientation reference. In addition, they use a time-compensated sun compass to maintain a constant southerly direction even though the azimuthal position of the sun changes over the course of a day (Froy et al., 2003; Mouritsen and Frost, 2002). While monarchs use the sun as their primary orientation cue, they can also use the pattern of polarized light in the sky to navigate. Desert locusts are also known to use the both of these cues during their mass displacements (Homberg, 2015).

While flies do not perform mass migrations like monarchs or desert locusts, laboratory experiment showed flies can also use the sun (Giraldo et al., 2018) and skylight polarization (Weir and Dickinson, 2012) as an orientation reference. While monarch butterflies use a sky compass to migrate in a specific direction, fruit flies followed straight courses in randomly chosen directions relative to a simulated sun. This navigation strategy of maintaining a constant heading relative to a fixed, distant landmark, is named ‘menotaxis’.

The laboratory experiments (Giraldo et al., 2018) showed flies do not compensate their sky compass to adjust for the azimuthal motion of the sun during the day, but can maintain a constant heading relative to the it for a few hours. This strategy would allow an individual to fly straight for a few hours which would be sufficient for long-distance displacement. Similarly to fruit flies, ball-rolling dung beetles also use celestial cues to travel in a straight line (Dacke et al., 2013; el Jundi et al., 2016). Upon finding a dung pile, they cut off a piece and roll it away along a straight line in a randomly chosen direction to escape competitors. To navigate efficiently, they utilize various celestial cues, including the sun, the moon (Dacke et al., 2004), polarized skylight (el Jundi et al., 2014), and Milky Way (Dacke et al., 2013) as orientation references.

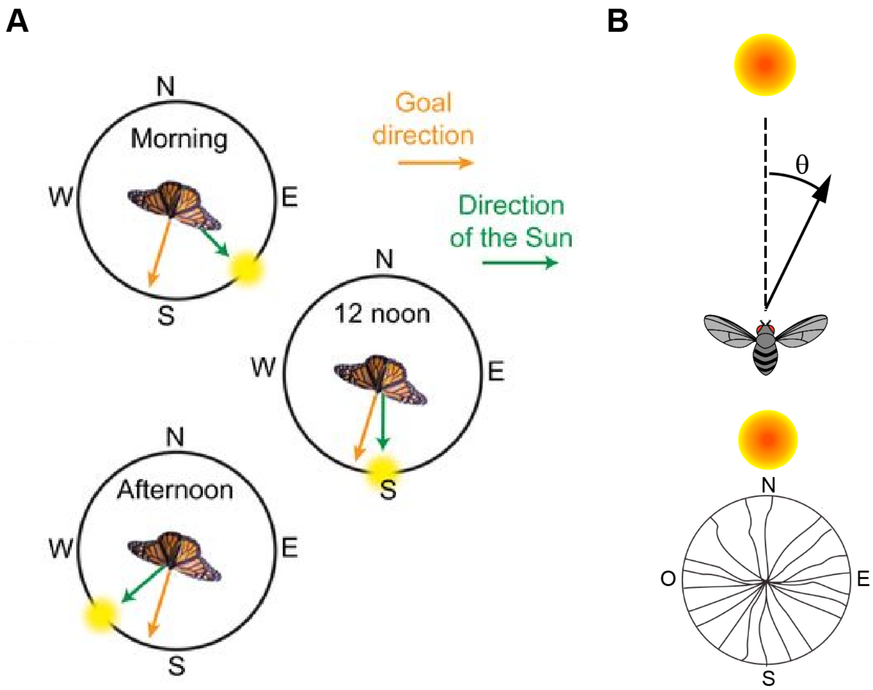

Figure 1.2: Insects use the sun as a compass for navigation.

(A) Monarch butterflies use the position of the sun combined with additional skylight cues to maintain their southward direction. In addition, they integrate time of day information to maintain a constant southerly direction even though the azimuthal position of the sun changes during the day. Figure reproduced from (Honkanen et al., 2019).

(B) Top: Orientation behavior of fruit flies in response to a simulated sun. Tethered flying flies show a menotactic orientation behavior to the ersatz sun. The letter theta, θ, indicates the angle between the cue and the fly's heading. Flies select different θ angles with respect to the sun and maintain it to move in a straight line.

Bottom: Each fly maintains a different flight direction (θ) to the ersatz sun. Example trajectories are shown in black. Figure modified from (Beetz and el Jundi, 2018).

Thus, insects can use a variety of celestial cues to perform long and short navigational tasks. Even though migratory behaviors are complex, they all involve comparison between the desired heading and the animal's current body orientation. If these two angles do not align, the animal needs to perform a compensatory turn (Honkanen et al., 2019). These navigational decisions have to be carried out on a moment-to-moment basis and are independent of the overall navigation strategy. Thus, sensory visual and motor information needs to be continually integrated, computed, and matched with the desired heading to elicit an appropriate goal-directed movement. The central complex, a very conserved region in the center of the insect's brain, has been shown to be necessary for all the behaviors described before, and much research in the last decade has focused on uncovering the neural basis of different navigational tasks in different insect species.

Experimental design of the release-and-recapture experiments

We aimed to perform our release-and-recapture in field site without vegetation or prominent geological features to limit the flies' visual and olfactory experience. We chose the dry bed of Coyote Lake in the Mojave Desert, which was large and sparce enough for us to position the traps at a one-kilometer radius from our release site (Figure 1.3A). In most experiments (n = 5), we positioned 10 traps at a radius of 1 km, except for one experiment, were we placed the traps at a radius of 250 m. The number of flies released in each experiment ranged from ~30,000 to 200,000, consisting of both males and females. During all the experiments, we monitored the wind speed and direction using an anemometer placed at the release site. We baited these traps using an apple ferment that was actively producing both CO_2 and ethanol, in addition to other volatile compounds. To further encourage flies' entry into the traps, we placed in the ferment a small container of pureed banana, as both a landing site and a source of odors. Each trap surface consisted of a loose-woven fabric with inwardly pointing funnels used to trap the flies once they ventured in (Figure 1.3B). Our traps differed most significantly from those set out by Coyne and coworkers (Coyne et al., 1982) in that they were outfitted with cameras, aimed downward at the trap surface, to record the arrival of flies to each trap (Figure 1.3C). The flies' arrival data gave us confidence that our captured flies were, indeed, the same flies we had released, as our cameras showed stereotyped "waves" of fly arrivals that always occurred after the simultaneous release of our flies. Furthermore, having these timestamps of flies' arrivals allowed us to analyze their total flight times, allowing us to test various models of wind-assisted dispersal behavior.

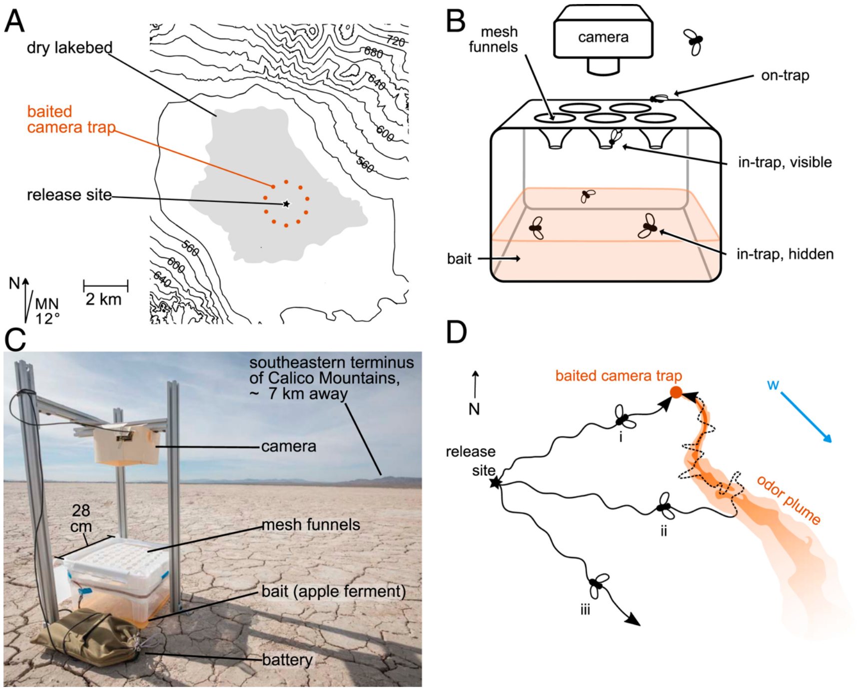

Figure 1.3: Experimental design.

(A) The experiments were conducted at Coyote Lake (gray), a dry lakebed in the Mojave Desert. Contours are in meters. We typically used 10 baited camera traps (orange) at a radius of 1 km from the release site (black star). North, N; magnetic north, MN.

(B) Cartoon of trap, dimensions not to scale. The top mesh surface contained an array of funnels projecting inward toward the bait. Only five funnels are drawn; the actual traps had 60 funnels. The camera captures time-lapse images, monitoring the number of flies atop the trap (on-trap) and directly underneath the mesh top (in-trap, visible). The camera cannot detect flies deeper inside (in-trap, hidden).

(C) Trap deployed on lakebed.

(D) Key assumptions guiding experimental design. Wind (blue vector) advects a turbulent odor plume (orange) from each trap. Flies whose trajectory from the release site happens to intersect the plume near a trap (i) are likely to be among the earliest arrivers, owing to their relatively direct path. Flies that intercept a plume downwind of its source (ii) will follow a longer path before arriving at the trap (broken line). Many flies will not encounter a detectable plume (iii). Figure reproduced from (Leitch et al., 2021).

By monitoring each trap with a camera, we were able to measure flies' overall flight times to draw inferences about the trajectories they followed on the way to the trap. We needed some framework for modeling the flies' behavior during the minutes between release and recapture, and had to make some assumptions: given that the release site was a full kilometer away from any trap, and that the traps were far apart, we assumed that only a very small subset of recaptured flies would select a trajectory leading them directly to a trap. We reasoned that most of our recaptured flies would arrive at a trap by first intersecting a trap's odor plume, and then tracking the plume upwind to its source. Thus, we envisioned our trap-count distributions to reflect two processes comprising distinct behavioral algorithms: (1) a dispersal phase before the fly detects an odor, and (2) a plume-tracking phase (Figure 1.3D).

While the search algorithm flies use to track odors has not been studied in the field, experiments in flight arenas and wind tunnels show flies follow a characteristic sequence of behaviors to track the source of an odor (Budick and Dickinson, 2006; van Breugel and Dickinson, 2014) (Figure 1.4). Upon encountering an odor filament, they quickly surge upwind. If they lose the odor, they execute a crosswind cast flying perpendicular to the direction of flow, which allows the fly to reenter the plume. As the fly gets close to the target, it is visually attracted to the odor source. This strategy is known as "cast-and-surge".

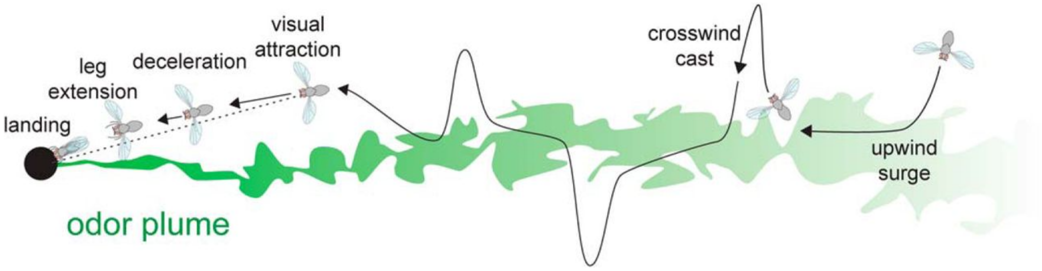

Figure 1.4: Plume tracking behavior.

When a fly encounters an odor, it initiates an upwind surge, flying parallel to the wind direction. If the fly losses the odor, it performs a crosswind cast flying perpendicular to the direction of flow, which allows it to reenter the plume. As the fly gets close to the target, it is visually attracted to the odor source. Figure reproduced from (Baker et al., 2018).

1.3 Results

The number of individuals captured in the traps shows flies have some capacity to travel in upwind and crosswind directions

Without relying on the camera data, we could see that average windspeed during each experiment shaped the distribution of final trap counts in a systematic manner: low winds yielded a more uniform distribution of trap counts, while high wind speeds biased trap counts downwind (Figure 1.5A and B). Despite this strong effect, in all but the windiest conditions, we always observed at least some flies at the cross and upwind traps, demonstrating that these small flies released in the desert were not simply being passively advected by the wind. This helped us recognize that, to model *Drosophila* dispersing in open environments, we would need to consider more than just advection and diffusion.

To determine if *Drosophila* actively regulate their groundspeed during dispersal, we compared arrival dynamics at downwind and upwind traps. Because of the difficulties in recording flies' flight trajectories as they approached the traps, we recognized that this study would not be able to directly address plume-tracking behaviors. Knowing this, we focused our analyses on those flies whose trajectories were most likely to have been dominated by the dispersal phase, with negligible amounts of plume tracking. To do this, we focused our analyses on a small subset of flies, termed "first arrivers," assuming that these flies were individuals whose trajectories across the open lakebed happened to, by chance, lead them directly to a trap with very minimal need for plume-tracking (Figure 1.3 D, trajectory i). This analysis was conducted on data collected from an experiment using a circular array of traps positioned 250 m from the release site, because the higher proportion (~2%) of flies recaptured at this shorter distance provided more arrival events. We pooled the camera data collected from the traps into two groups, representing the downwind and upwind sectors. Although the pooled data from upwind and downwind traps differed with respect to the total number of flies captured, the time courses were remarkably similar (Figure 1.6).

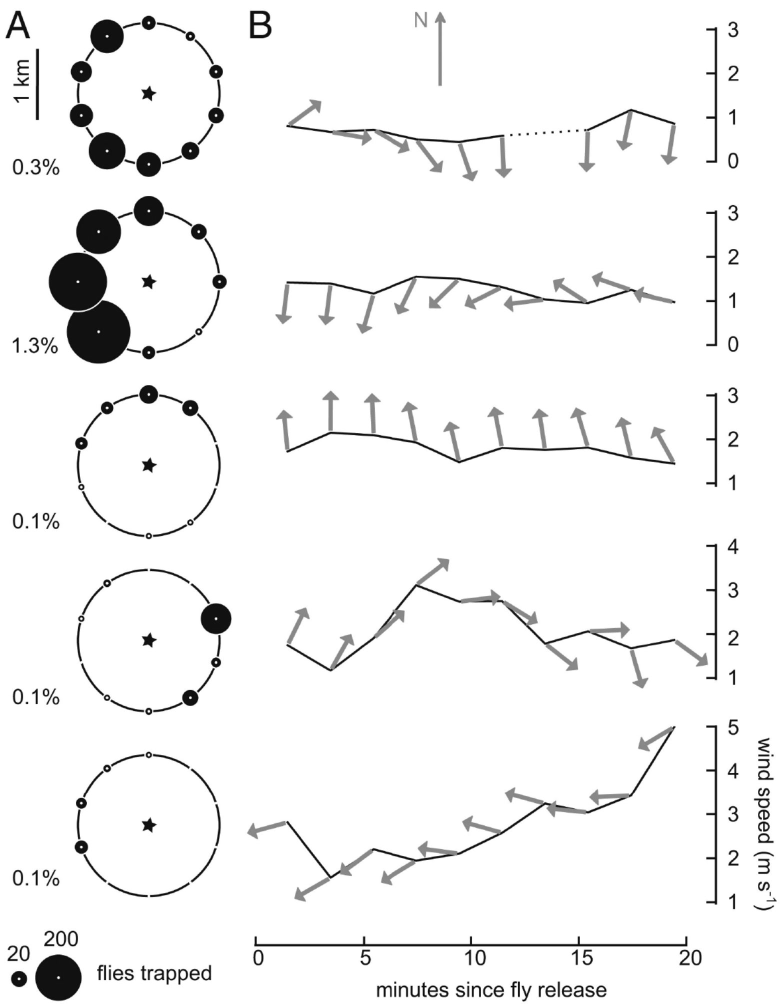

Figure 1.5: Influence of wind on circular distribution of trapped flies.

(A) Data from traps positioned 1 km away from the release site. Each row depicts the results of a different release. The area of each black circle indicates the number of flies caught in that trap by the end of each experiment. The five experiments are ordered according to the vector-averaged windspeed over the first 20 min following release. Recapture percentages, calculated using estimates of release populations, are indicated at the bottom left of each panel.

(B) Windspeed and direction during the releases. Data were vector averaged in 2 min bins. Arrow lengths are fixed and point downwind; the position of each arrow's base along the ordinate indicates vector-averaged windspeed.

Figure reproduced from (Leitch et al., 2021).

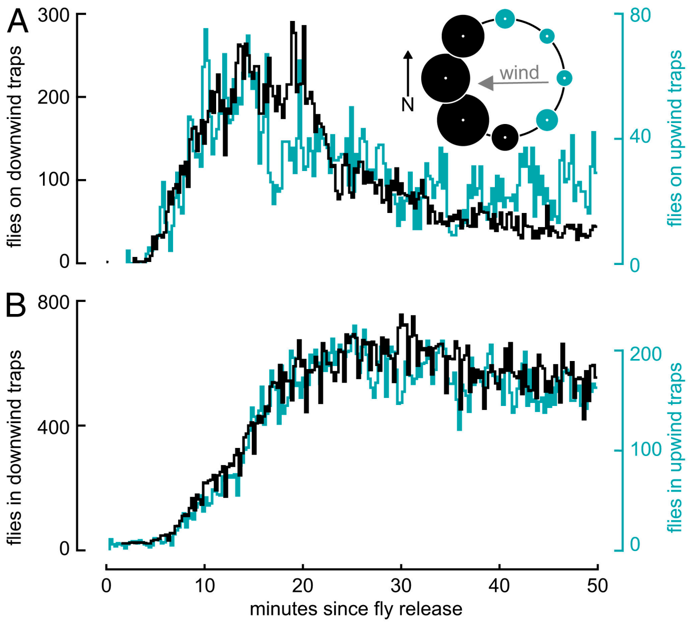

Figure 1.6: In moderate winds, *Drosophila* regulate groundspeed.

(A) During this experiment, traps were positioned at a 250 m radius from the release site. The vector-averaged windspeed was 1.5 m s^{-1}, almost due east (gray arrow). We define four traps as upwind (cyan circles) and four as downwind (black circles). The number of flies imaged on the trap surface (black), summed across all downwind traps for each time bin, is shown with the number of flies imaged on top of all upwind traps (cyan; note difference in scale).

(B) From the same experiment, the number of flies visible within the upwind and downwind traps.

Figure reproduced from (Leitch et al., 2021).

By analyzing the data from experiments using traps set at 1 km, we could derive better estimates of flies' groundspeeds as well as examine the influence of the wind more accurately. As with the 250 m data, we manually annotated the camera images to find the first arrivers. Thirty different traps from the five experiments were amenable to this analysis. Using the arrival times of the flies that first arrived to the traps, we estimated the average groundspeed along the trajectory from release site to trap, g_{traj}. From anemometer data, we determined the average headwind or tailwind that these first arrivers would have experienced during their flights, w_{traj} (Figure 1.7A). Plotting g_{traj} against w_{traj} indicates the influence of the wind conditions (Figure 1.7B). If the flies were simply advected by the wind, all the data should lie on a line running through the origin, with a slope of one. If the flies compensated groundspeed perfectly, then the data should fall about a horizontal line representing the average preferred groundspeed value. The distribution of field data suggests an intermediate behavior; flies exhibit some ability to actively regulate groundspeed at low windspeeds but tend to move with the wind as windspeed increases (Figure 1.7C). Two data points showed unusually large values for groundspeed, and we suspect that these outliers were due to misidentification of some local fly-sized insects in our annotations.

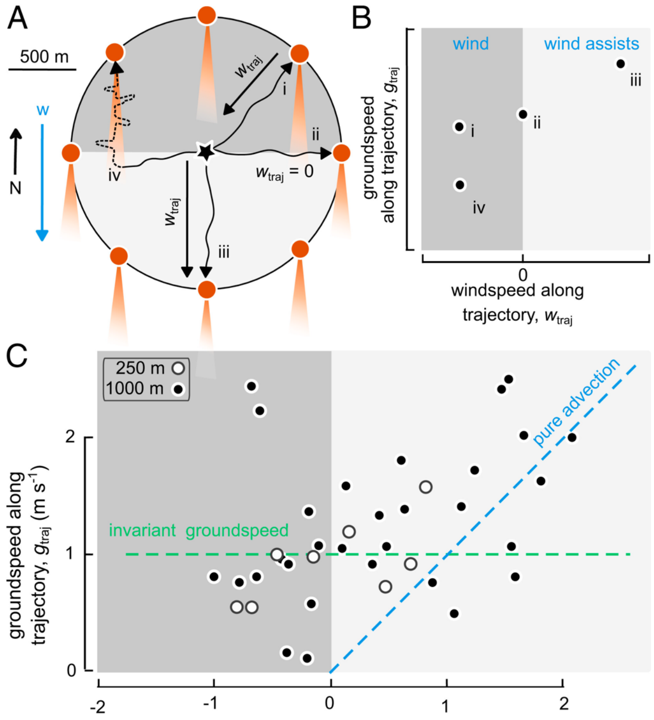

Figure 1.7: Relationship between groundspeed and windspeed.

(A) Hypothetical trajectories of four flies. Black vectors show the component of wind parallel to flight trajectories (w_{traj}).

(B) For each fly in A, groundspeed along the trajectory (g_{traj}) is plotted as a function of w_{traj}. The value of g_{traj} will be underestimated for flight paths that do not intercept a plume near the trap (fly iv). Negative w_{traj} values (dark gray) denote trajectories opposed by the wind; positive (light gray) indicate trajectories assisted by wind.

(C) Field measurements of g_{traj} and w_{traj}, from 30 1,000 m traps over the five experiments shown (black circles), superimposed with the relationships expected if flies were entirely advected by wind (blue) or maintained some preferred groundspeed (green). The white circles show comparable values of g_{traj} and w_{traj} derived from the 250 m trap experiment shown in Figure 1.6.

The cluster of groundspeed values measured when w_{traj} was near zero and provides a rough estimate of the preferred groundspeed that flies use in the absence of any wind. This value, $\sim 1\ \mathrm{m\ s^{-1}}$, is much higher than measurements of *Drosophila* flight velocities made in indoor wind tunnels (Medici and Fry, 2012; Straw et al., 2010), but consistent with values made for flies flying in greenhouses (Combes et al., 2012). The high value for estimated groundspeed suggests that the flies, the first arrivers at least, must have flown in rather straight trajectories between the release site and traps. If they had executed highly meandering paths, they could not have reached the traps at the recorded times using flight speeds that are biomechanically feasible.

Proposing a dispersal model

Thus far, our results suggest that flies fan out in different directions when released, with at least some flies maintaining a roughly straight trajectory. Two basic mechanisms might explain how they maintain a straight path as they disperse. In the first, each fly chooses at random a constant heading (i.e., body orientation) relative to a celestial cue (Figure 1.2). In the second, flies somehow actively maintain a constant trajectory (i.e., a straight path over the ground), perhaps by orienting to a distant visual landmark (Götz, 1987). These two hypotheses are distinct because a flying animal can move such that its longitudinal body axis (heading) is not aligned with its groundspeed vector (trajectory). Thus, an animal might maintain a constant heading while its trajectory varies or maintain a constant trajectory while its heading varies.

To account for the influence of the wind, we propose a simple set of behavioral algorithms that collectively constitute an agent-based model that could explain the key features of our field data and is consistent with prior laboratory observations (Figure 1.8, Model 1). In our model, each fly maintains a constant heading and regulates groundspeed, but the groundspeed regulator, only operates on the velocity component oriented along the body axis. In other words, flies do not regulate sideslip but rather allow themselves to be advected sideways. Note, our analysis is based on measurements of the first arrivers—that we assume were lucky to choose a heading that carried them almost directly to a trap—and makes no attempt to model the complex phenomena associated with plume tracking.

We then developed a set of four agent-based models that all incorporated unregulated sideslip, but with different variations, thus creating a 2 × 2 matrix of two binary assumptions: 1) fixed random heading versus fixed random trajectory and 2) regulated longitudinal groundspeed versus unregulated groundspeed. We then simulated the relationship between w_{traj} and g_{traj} (to generate a plot similar to the one shown in 1.7C), simulated over a range of windspeeds and wind directions. These simulations generate distinct relationships between the two field-measurable parameters (Figure 1.8). To quantitatively compare the performance of these different models, we calculated the average pair-wise log likelihood ratio between Model I and each of the alternate models, determined using 40,000 bootstrap iterations. The resultant distributions of log likelihood ratios indicate that Models 1 and 3—both of which invoke groundspeed regulation—predict our field data equally well, in contrast to Models 2 and 4, which lack groundspeed regulation.

Collectively, these results suggest that a relatively simple behavioral algorithm involving either fixed random heading or trajectory, regulated groundspeed, and unregulated sideslip can account for the salient features of dispersal behavior under a range of different wind conditions.

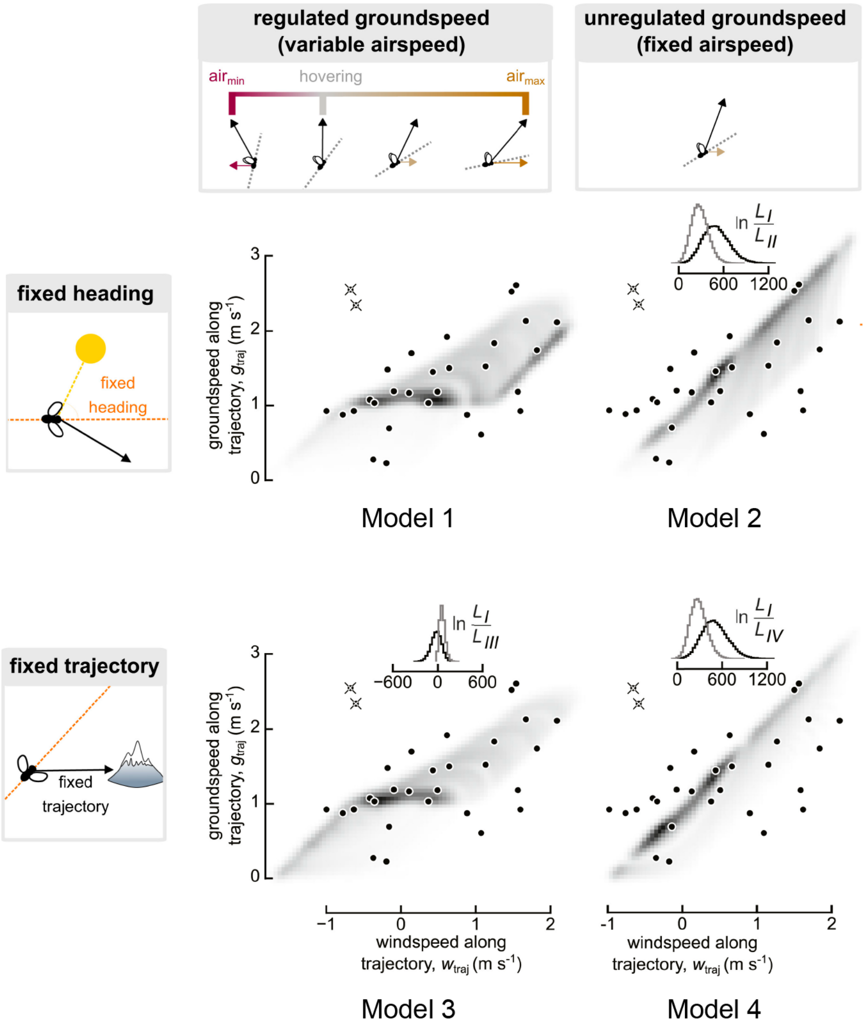

Figure 1.8: Four behavioral models of wind-assisted dispersal.

The relationship between w_{traj} and g_{traj}, simulated over a range of windspeeds and wind directions. The four behavioral models, simulated over a wide range of wind conditions, generate distinct relationships between the two field-measurable parameters. Grayscale shading shows each models' normalized probability density function (PDF). Field measurements are plotted over each model's PDF; likelihood values at each point were compared pairwise between models. Insets: show the bootstrapping of the field data over 40,000 iterations generated a distribution of log likelihood ratios comparing each model vs. Model I.

A simple advection-diffusion model does not recapitulate the dispersal behavior

To compare our results with more traditional, analytic models of insect dispersal (Kareiva, 1983), we also simulated the expected distribution of g_{traj} and w_{traj} of flies arriving at a ring of traps if governed by the advection–diffusion equation. We initially calculated a rough estimate by noting that the rms displacement, R, of a particle moving by diffusion in the absence of advection is given by equation 1.1 as follows:

$$R = \sqrt{4DT}, \tag{1.1}$$

where D is the diffusion constant and T is the time taken to reach R. We can rearrange this expression as $R/T = 4D/R$ and estimate R/T (which has units of velocity) as the flies' preferred groundspeed at zero windspeed ($\sim$1 m s^{-1}). This calculation yields a diffusion coefficient of $\sim$250 m^2 s^{-1} for the 1 km trap data but a value of $\sim$62 m^2 s^{-1} for the 250 m trap data. This simple analysis suggests that data collected at 250 m and 1 km cannot be described by a single diffusion coefficient. To be governed by the same diffusivity, the flies arriving at the 250 m traps would have had to have flown approximately four times faster, or the flies arriving at the 1 km traps would have had to have flown $\sim$0.25 times slower. What we instead observed is that flies used the same preferred groundspeed independent of the spatial scale of the experiment (Figure 1.7). These results were further validated by performing a simulation of the release-and-recapture data using advection–diffusion model (data not shown here).

1.4 Discussion

These results provide evidence that an agent-based model in which flies maintain a constant heading and preferred longitudinal ground speed while not regulating sideslip can explain salient features of dispersal in an open landscape. Agent-based models in which each animal follows a finite set of rules are not necessarily incompatible with statistical models such as the advection–diffusion equation, in which animals move according to a random Brownian process. However, in this particular case, the behavior of the first arriver flies at our field traps was not consistent with Brownian motion because flies appear to maintain a preferred groundspeed that is scale independent. While not negating the utility of advection–diffusion models in describing insect motion under many conditions—in a more spatially complicated, sensory landscape, for example—our results suggest that when released in an open area, *Drosophila* execute a set of behavioral algorithms that appear largely optimized for long-distance dispersal rather than local search.

Our results indicate that dispersing *Drosophila* actively regulate their longitudinal groundspeed to a value of ∼1 m s^{-1}. Fully fed, tethered flies can fly for up to 3 h (Götz, 1987), a value that is consistent with measurements of metabolic rate and aerodynamic power requirements (Lehmann and Dickinson, 1997). This suggests that a single fly could cover ∼12 km without the need for refueling, a distance of about 4.8 million body lengths. Even if this value represents an extreme performance estimate, it nevertheless demonstrates a surprising dispersal capacity for a small, 1 mg insect. At the higher groundspeeds we measured under windy conditions (∼2.5 m sec^{-1}), the dispersal distance estimate for a single flight increases to ∼30 km. Flies could almost certainly disperse much further in an uncontrolled fashion in more extreme conditions, especially if they were carried well above the boundary layer into higher elevations where they catch prevailing winds (Reynolds et al., 2017).

Many animals localize food by moving upwind within advected odor plumes (Baker et al., 2018), a behavior termed odor-mediated anemotaxis. This behavior typically involves an iterative sequence of upwind surges when odor is detected, interspersed with crosswind casts when the odor is lost (Figure 1.4). Although we could not directly observe plume tracking in our field experiments, *Drosophila* readily exhibit such behavior in wind tunnels (van Breugel and Dickinson, 2014). Whereas the utility of the cast-and-surge algorithm is obvious once an animal encounters a plume, the best strategy before it detects an odor is less clear and may depend on wind conditions (Dusenbery, 1989) and—just as importantly—on the natural history of each particular species. Some insects, such as the cabbage root fly, fly upwind when experiencing an odorless background flow (Finch and Skinner, 1982). This might seem logical, simply because if an animal detects an odor, its source must be upwind. On the other hand, by flying upwind, an animal limits itself to odor targets that reside in a narrow sector directly ahead. In our experiments, we observed that *Drosophila* fan out in all directions at low windspeeds, while at higher speeds, the flies were biased downwind. The behavior we observed, and the model we propose, may be viewed as a compromise between the need to find an attractive odor plume and the goal of using the wind to increase dispersal distance. By not regulating sideslip, the flies allow themselves to be directed downwind, but by regulating longitudinal groundspeed, they maintain some crosswind component that might increase the probability of encountering an upwind plume.

Although we captured flies at odor-baited traps, there is some possibility that the flies arrived without having tracked its associated plume upwind. If 100,000 flies fanned out evenly in all directions from the release site, they would reach the perimeter of the trap radius at a linear density of ∼16 flies per meter. If we liberally assume that a fly might be able to see a trap from a distance of 10 m, then it is possible that ∼320 flies would pass near enough to a trap that they might land on it without needing to follow the odor plume. Thus, we may have only trapped flies that happened to choose trajectories that carried them near one of the traps. There are several arguments against this interpretation. First, our coarse estimates for how many flies came within the visual detection range of the traps are almost certainly an overestimate as it assumes that all the flies flew within 1 to 2 m of the ground where they could encounter the trap. *Drosophila* spp. have been observed at high density in 200 m–high aerial traps (Chapman et al., 2011), and it is possible that many of the flies in our experiments rose well above the ground after release. Second, laboratory experiments indicate that flying flies are not attracted to land on visual objects until after they have encountered an attractive odor (van Breugel and Dickinson, 2014); it thus seems reasonable to assume that the flies would have made some contact with the plume before landing on the trap.

Of the agent-based models we tested, the two that combined longitudinal groundspeed regulation with either fixed heading or fixed trajectory (Models 1 and 3) performed best in predicting our field data. Of these two, we believe that the fixed heading model is the most biologically plausible as this is consistent with laboratory experiments showing that flies adopt arbitrary headings relative to patterns of skylight polarization and sun position. Tethered *Drosophila* do steer toward large conspicuous visual objects (Kareiva and Shigesada, 1983)—a reflex called stripe fixation. However, although the lakebed is surrounded by some ridges (Figure 1.3), none contain vertical features that seem prominent enough to elicit a strong fixation response from the release site. Further, a fixation response to one or two geological features could not easily explain how flies fan out in many directions.

Dispersing *Drosophila* use celestial cues not as a compass to go in a preferred direction but rather simply as a means of holding an arbitrary orientation (i.e., menotaxis). In this regard, flies' use of the sky compass system is similar to dung beetles, which maintain a straight trajectory away from the dung pile (Dacke and El Jundi, 2018), but not like monarch butterflies, which use the sun compass to fly in a particular direction (see Figure 1.2).

We deliberately chose to conduct our experiments on a flat, featureless, dry lakebed to simplify the external factors that might influence dispersal behavior; however, we acknowledge that our experiments were artificial in a number of ways. First, *D. melanogaster* is a cosmopolitan species that originated in Africa. Thus, we can infer little regarding the species-specific behavior of the flies as it relates to their ancestral habitat. Instead, our observations more likely shed light on deeply rooted behavioral algorithms that are shared by many insects and not the result of recent evolutionary processes (Dickinson, 2014). Second, our experiments forced a rapid, mass exodus, whereas dispersal within the normal life history of flies is more likely a choice influenced by a complex interaction of internal and external factors (Zera and Denno, 1997).

In summary, we propose a model of wind-assisted dispersal in which each insect chooses and maintains a random heading and regulates its longitudinal groundspeed but tolerates wind-induced sideslip. While undoubtedly simplistic, the advantage of our model is that it can explain dispersal behavior under a variety of wind conditions without requiring that any individual animal change its behavioral set point as a function of windspeed. It thus represents a biologically feasible “rule-of-thumb” that yields a desired behavioral outcome without requiring sophisticated neural computations. Although derived from measurements on *Drosophila*, we suggest that the model might explain the dispersal behavior of many flying insects with roughly similar natural histories.

1.5 Materials and methods

For detailed materials and methods, see the Supplemental information in (Leitch et al., 2021).

Fly Release and Recapture.

We performed a series of release-and-recapture experiments using a population of laboratory-reared *D. melanogaster* on a dry lakebed (Coyote Lake) in the Mojave Desert. We deployed a circular ring of traps, each equipped with a downward-facing camera (Raspberry Pi) and baited with fermenting apple juice. In five experiments, we positioned 10 traps at a radius of 1 km; in one preliminary experiment, we placed the traps at a radius of 250 m. The mesh surface of the traps contained an array of inwardly pointed funnels, allowing us to count and identify the flies at the end of each experiment. An anemometer (Met One, direction sensor 020C, speed sensor 010C) placed at the release site recorded the time course of windspeed and direction in each experiment. The number of flies released in each experiment ranged from ~30,000 to 200,000. In addition to counting the flies that had arrived at each trap, we also scored the arrival times of the first flies to land on each trap via manual inspection of time-stamped camera images and in some cases using custom-written machine vision software (https://github.com/kateleitch/drosophila_wind_assisted_dispersal).

Agent-Based Models.

To help interpret our results, we developed agent-based models in which each fly maintains a random constant azimuthal orientation but is advected sideways by the wind. We developed four different models that all incorporated unregulated sideslip but differed with respect to whether the flies maintained a constant heading or constant trajectory and whether they regulated longitudinal groundspeed or not. We simulated the output of the models using ~45,000 permutations in which each fly chose a different heading or trajectory and was subjected to a wind magnitude derived from a distribution based on our field measurements

References

Baker, K. L., Dickinson, M., Findley, T. M., Gire, D. H., Louis, M., Suver, M. P., Verhagen, J. V., Nagel, K. I. and Smear, M. C. (2018). Algorithms for Olfactory Search across Species. J. Neurosci. 38, 9383–9389.

Beetz, M. J. and el Jundi, B. (2018). Insect Orientation: Stay on Course with the Sun. Current Biology 28, R933–R936.

Budick, S. A. and Dickinson, M. H. (2006). Free-flight responses of Drosophila melanogaster to attractive odors. J Exp Biol 209, 3001–3017.

Chapman, J. W., Drake, V. A. and Reynolds, D. R. (2011). Recent Insights from Radar Studies of Insect Flight. *Annu. Rev. Entomol.* 56, 337–356.

Cheung, A., Zhang, S., Stricker, C. and Srinivasan, M. V. (2007). Animal navigation: the difficulty of moving in a straight line. *Biol Cybern* 97, 47–61.

Combes, S. A., Rundle, D. E., Iwasaki, J. M. and Crall, J. D. (2012). Linking biomechanics and ecology through predator–prey interactions: flight performance of dragonflies and their prey. *Journal of Experimental Biology* 215, 903–913.

Coyne, J. A., Boussy, I. A., Prout, T., Bryant, S. H., Jones, J. S. and Moore, J. A. (1982). Long-Distance Migration of Drosophila. *The American Naturalist* 119, 589–595.

Dacke, M. and El Jundi, B. (2018). The Dung Beetle Compass. *Curr Biol* 28, R993–R997.

Dacke, M., Byrne, M. J., Scholtz, C. H. and Warrant, E. J. (2004). Lunar orientation in a beetle. *Proceedings of the Royal Society of London. Series B: Biological Sciences* 271, 361–365.

Dacke, M., Baird, E., Byrne, M., Scholtz, C. H. and Warrant, E. J. (2013). Dung beetles use the Milky Way for orientation. *Curr Biol* 23, 298–300.

David, C. T. (1978). The relationship between body angle and flight speed in free-flying Drosophila. *Physiological Entomology* 3, 191–195.

Dickinson, M. H. (2014). Death Valley, Drosophila, and the Devonian Toolkit. *Annual Review of Entomology* 59, 51–72.

Drake, V. A. and Gatehouse, A. G. (1995). *Insect Migration: Tracking Resources Through Space and Time*. Cambridge, UK: Cambridge University Press.

Dusenbery, D. B. (1989). Optimal search direction for an animal flying or swimming in a wind or current. *J Chem Ecol* 15, 2511–2519.

el Jundi, B., Smolka, J., Baird, E., Byrne, M. J. and Dacke, M. (2014). Diurnal dung beetles use the intensity gradient and the polarization pattern of the sky for orientation. *Journal of Experimental Biology* 217, 2422–2429.

el Jundi, B., Foster, J. J., Khaldy, L., Byrne, M. J., Dacke, M. and Baird, E. (2016). A Snapshot-Based Mechanism for Celestial Orientation. *Current Biology* 26, 1456–1462.

Finch, S. and Skinner, G. (1982). Upwind flight by the cabbage root fly, Delia radicum. *Physiological Entomology* 7, 387–399.

Froy, O., Gotter, A. L., Casselman, A. L. and Reppert, S. M. (2003). Illuminating the Circadian Clock in Monarch Butterfly Migration. *Science* 300, 1303–1305.

Fuller, S. B., Straw, A. D., Peek, M. Y., Murray, R. M. and Dickinson, M. H. (2014). Flying Drosophila stabilize their vision-based velocity controller by sensing wind with their antennae. *Proceedings of the National Academy of Sciences* 111, E1182–E1191.

Giraldo, Y. M., Leitch, K. J., Ros, I. G., Warren, T. L., Weir, P. T. and Dickinson, M. H. (2018). Sun Navigation Requires Compass Neurons in Drosophila. *Current Biology* 28, 2845-2852.e4.

Götz, K. G. (1987). Course-Control, Metabolism and Wing Interference During Ultralong Tethered Flight in Drosophila Melanogaster. *Journal of Experimental Biology* 128, 35–46.

Homberg, U. (2015). Sky Compass Orientation in Desert Locusts—Evidence from Field and Laboratory Studies. *Front. Behav. Neurosci.* 9,.

Honkanen, A., Adden, A., da Silva Freitas, J. and Heinze, S. (2019). The insect central complex and the neural basis of navigational strategies. *Journal of Experimental Biology* 222, jeb188854.

Jones, J. S., Bryant, S. H., Lewontin, R. C., Moore, J. A. and Prout, T. (1981). Gene flow and the geographical distribution of a molecular polymorphism in Drosophila pseudoobscura. *Genetics* 98, 157–178.

Kareiva, P. M. (1983). Local movement in herbivorous insects: applying a passive diffusion model to mark-recapture field experiments. *Oecologia* 57, 322–327.

Kareiva, P. M. and Shigesada, N. (1983). Analyzing insect movement as a correlated random walk. *Oecologia* 56, 234–238.

Lehmann, F. O. and Dickinson, M. H. (1997). The changes in power requirements and muscle efficiency during elevated force production in the fruit fly Drosophila melanogaster. *J Exp Biol* 200, 1133–1143.

Leitch, K. J., Ponce, F. V., Dickson, W. B., van Breugel, F. and Dickinson, M. H. (2021). The long-distance flight behavior of Drosophila supports an agent-based model for wind-assisted dispersal in insects. *Proceedings of the National Academy of Sciences* 118, e2013342118.

Medici, V. and Fry, S. N. (2012). Embodied linearity of speed control in Drosophila melanogaster. *J R Soc Interface* 9, 3260–3267.

Merlin, C., Heinze, S. and Reppert, S. M. (2012). Unraveling navigational strategies in migratory insects. *Curr Opin Neurobiol* 22, 353–361.

Mouritsen, H. and Frost, B. J. (2002). Virtual migration in tethered flying monarch butterflies reveals their orientation mechanisms. *Proceedings of the National Academy of Sciences* 99, 10162–10166.

Reppert, S. M. and Roode, J. C. de (2018). Demystifying Monarch Butterfly Migration. *Current Biology* 28, R1009–R1022.

Reynolds, D. R., Chapman, J. W. and Drake, V. A. (2017). Riders on the Wind: The Aeroecology of Insect Migrants. In *Aeroecology* (ed. Chilson, P. B.), Frick, W. F.), Kelly, J. F.), and Liechti, F.), pp. 145–178. Cham: Springer International Publishing.

Straw, A. D., Lee, S. and Dickinson, M. H. (2010). Visual Control of Altitude in Flying *Drosophila*. *Current Biology* 20, 1550–1556.

van Breugel, F. and Dickinson, M. H. (2014). Plume-tracking behavior of flying Drosophila emerges from a set of distinct sensory-motor reflexes. *Curr Biol* 24, 274–286.

Weir, P. T. and Dickinson, M. H. (2012). Flying *Drosophila* Orient to Sky Polarization. *Current Biology* 22, 21–27.

Zera, A. J. and Denno, R. F. (1997). Physiology and Ecology of Dispersal Polymorphism in Insects. *Annu. Rev. Entomol.* 42, 207–230.

Chapter 2

BEHAVIORAL CHARACTERIZATION OF THE INTEGRATIVE FEATURES OF THE OPTOMOTOR RESPONSE IN FLYING *DROSOPHILA*

2.1 Abstract

Flying insects, such as *Drosophila melanogaster*, need to continuously adjust their flight trajectory to compensate for perturbations. These adjustments can be discrete, rapid steering maneuvers to avoid collisions or predators, or continuous fine-scaled changes in motor output to account for developmental or damage-induced asymmetries of the wings and body. Because aerodynamic torque increases exponentially with wing length, minor asymmetries in wing size can produce significant asymmetrical aerodynamic forces and torques. Without compensation, these would quickly cause the insect to spiral off course. Whereas insects use many different sensory modalities to detect perturbations, they rely extensively on optic flow to modify their motor output and remain on course. The optomotor response is a well-studied behavior in flies in which the insect compensates for deviations from a straight flight path by steering in the direction of wide-field visual motion, reducing the apparent rotation of the visual scene on its retina. The optomotor response is understood as a form of trimming the motor system to account for a locomotory bias due to either internal or external perturbations. I examined the optomotor response of tethered flies in a virtual reality arena where flies were able to freely rotate in yaw. To mimic a locomotory bias, I exposed flies to wide-field visual motion in the yaw direction. As expected, presentation of wide-field yaw stimulus induced the characteristic optomotor response, in which flies maintained a constant angular velocity to follow the visual motion. Thus, the flies altered their motor output to compensate for a perceived locomotory bias. I observed that after the cessation of the moving stimulus, flies maintained the elicited angular velocity for several minutes. I then applied a control theoretic

framework and determined that a proportional-integral controller, a model commonly used in engineering, best explains the behavior observed during the flies' yaw optomotor response. However, the estimated integral gain is small; thus I performed simulations that exemplify the potential functional advantage of this controller model in the insect's natural flight behaviors.

2.2 Introduction

Flying insects can navigate along a relatively straight path for long distances (Chapman et al., 2015; Götz, 1987; Leitch et al., 2021). In order to do so, they must continuously adjust their flight trajectory to compensate for internal or external perturbations (Dickinson and Muijres, 2016). These adjustments can be discrete, rapid steering maneuvers to avoid collisions or predators (Dickinson, 2005; Tammero and Dickinson, 2002), or continuous fine-scaled changes in motor output to account for developmental or damage-induced asymmetries of the wings and body. An insect with unilateral wing damage, for example, would generate asymmetrical aerodynamic forces and torques that, if left uncompensated, could cause it to quickly spiral off course (Muijres et al., 2017; Salem et al., 2022). Because aerodynamic torque is roughly proportional to the fifth power of wing length (Ellington and Lighthill, 1997), even small asymmetries in wing size require the maintenance of bilateral differences in wing motion to maintain a stable trajectory. Straight flight is only possible because insects can account for perturbations by maintaining subtle bilateral differences in wing motion, constantly regulated by sensory feedback. Whereas insects use several sensory modalities to detect perturbations, they rely extensively on visual feedback (optic flow) to remain on course. The behavioral algorithms used to stabilize flight have been extensively studied in *Drosophila melanogaster* due to their robust behavior in tethered flight arenas and the ease of utilizing genetic tools. Thus, this is a convenient model in which to investigate the flexibility of the motor system during flight.

The optomotor response (OMR) is a well-studied behavior in flies in which the insect compensates for deviations from a straight flight path by steering in the direction of wide-field visual motion, reducing the apparent rotation of the visual scene on its retina (Götz, 1968). This stabilizing reflex has been extensively studied by measuring either the yaw torque generated by the fly (Götz, 1968; Götz et al., 1979), or the difference in bilateral wingbeat amplitudes (Tammero et al., 2004) induced by a wide-field stimulus.

The OMR is understood as a form of trimming the motor system to account for a locomotory bias due to either internal or external perturbations, and is often modeled using control theory (Figure 2.1) (Heisenberg and Wolf, 1984), in which the insect continually receives sensory input about its orientation and self-motion (e.g. rotational optic flow), and steers so as to minimize the magnitude of optic flow on its retina. In the feedback control diagram shown in Figure 2.1, I plot the visual system as the only sensory modality for simplicity, although flies are known to rely on other sensory systems for feedback, such as the halteres (Dickinson, 1999; Ristroph et al., 2010), and antennae (Fuller et al., 2014).

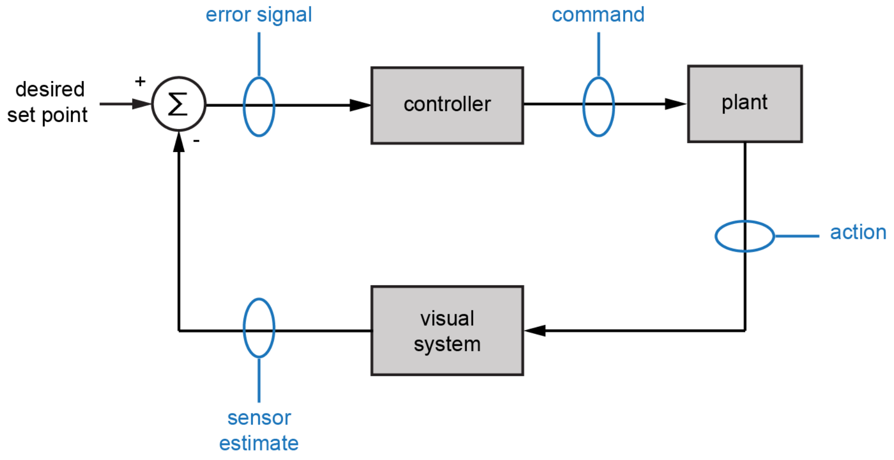

Figure 2.1: A block diagram illustrating a simplified feedback control loop for the yaw OMR. The system has a sensor, in this case the fly's visual system, that provides a measurement (e.g., the angular velocity of the visual scene). This estimate is then compared to a desired set point (e.g., zero angular velocity so as not to slip) to create an internal error signal or sideslip. This error signal is then processed using a particular algorithm by the controller to send a command to the plant, in this case, the fly, that then generates a compensatory motor response to continually minimize sideslip.

The yaw OMR is often studied in open-loop conditions in a flight simulator, in which the insect's motor actions are uncoupled from the visual input it experiences. In a typical open-loop experiment, an investigator presents a constantly rotating visual scene while measuring the fly's turning response. Work by Wolf and Heisenberg (1990), conducting open-loop OMR experiments, showed that after inducing flies to generate compensatory yaw torque via presentation of a constantly rotating visual scene, the flies' torque remained at the high state-state level for many seconds after the motion of the rotating pattern had stopped (Figure 2.2). This result suggested that the feedback controller of the OMR could be modeled as a proportional-integral (PI) feedback loop, a simple control system often used in engineering (Aström and Murray, 2021). In this control strategy, the fly's turning rate is proportional to the retinal slip perceived by the fly (which constitutes the error signal), plus the term proportional to the temporal integral of this same error signal. This control mechanism would allow the error signal to wind up over time, allowing the retinal slip to be minimized to zero, thus eliminating any locomotory bias, and explaining the observed persistent torque response that persists following the termination of visual motion.

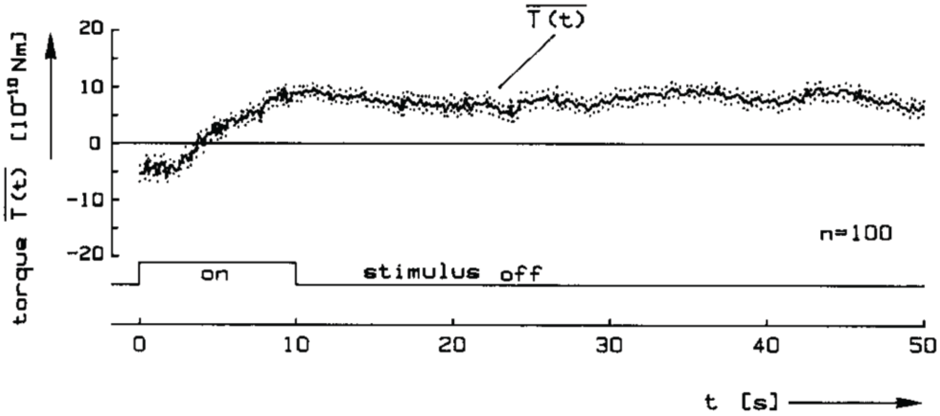

Figure 2.2: Demonstration of an integrator step in the OMR.

Average torque trace for a 10 s rotating stimulus (stimulus on), followed by a 40 s period where the pattern remained stationary (stimulus off). The solid line indicates the mean of means for all trials (100 trials collected from 7 individuals), and the dotted envelopes indicate the SEMs. Figure modified from Wolf and Heisenberg (1990), (Wolf and Heisenberg, 1990).

Schnell and coworkers (Schnell et al., 2014) measured the average stroke amplitude during an open-loop yaw OMR and, although the motor response after the termination of the visual stimulus decayed to zero after several seconds, in contrast to the Wolf and Heisenberg result. They proposed a neural mechanism to explain these slow, integrator-like dynamics of the OMR. However, an alternative way of investigating OMR is through the use of closed-loop conditions, in which the fly's motor actions control the pattern of optic flow it perceives, thereby simulating the feedback conditions experienced during free flight. In prior studies using a closed-loop paradigm, the yaw OMR is often modeled as a proportional feedback (P) controller (Cellini et al., 2022; Mongeau and Frye, 2017; Salem et al., 2022). Despite the lack of an integral feedback term, this simpler control model appears sufficient to explain the observed dynamics of closed-loop experiments. In this chapter, I present an extensive set of behavioral experiments aimed at determining which control model (P vs. PI) best approximates the behavior of the fly's intrinsic yaw OMR. I conclude that the fly's performance is better predicted by a PI control architecture, albeit with a very small integral gain term. Finally, I will discuss the potential functional advantages of PI feedback over P feedback in the natural flight behaviors of the fly.

2.3 Results

Flies maintain their optomotor response in the absence of visual stimuli

Prior research demonstrating that flies maintain a steering response after the termination of an open loop visual stimulus was conducted using a rigid tether such that flies lack that naturalistic sensory feedback from yaw rotation contributed by mechanosensory systems such as the halteres (Dickinson, 1999). In this study, I used a magnetic tether (magnotether) arena (Bender and Dickinson, 2006) in which the fly can freely rotate about its yaw axis to investigate the integrative characteristics of the OMR. I tracked the angular position of the fly's body axis in real-time, and presented the visual stimuli on a cylindrical LED arena surrounding the animal (Figure 2.3A). Initially, I tested the flies' optomotor OMR under closed-loop conditions by exposing flies to alternating periods of static visual scenes and rotating wide-field motion. I determined the flies' angular velocity traces using a Savitsky-Golay filter on the measured angular positions (Figure 2.3B). As expected, the rotating panorama elicited a smooth, co-directional optomotor turning response with occasional fast steering maneuvers called saccades. Because I am interested in studying how flies modulate steering to sustain straight flight over long timescales, and not during rapid turns, I identified saccades in the flies' trajectories and removed them from the angular velocity traces using previously described techniques (Ros et al., 2024). Upon presentation of a moving visual stimulus, flies quickly changed their angular velocity to match that of the visual scene in less than 1 s and maintained that angular velocity for the duration of the presentation (Figure

2.3D). During the periods in which the visual scene was static, flies maintained their mean angular velocity near zero, effectively stabilizing retinal slip. During periods in which I rotate the visual surround, I am effectively setting a rotatory bias, simulating a perturbation that the fly must compensate to achieve zero retinal slip. I rotated the visual scene at a constant angular velocity of 184.6 deg s^{-1}, and flies nearly matched the imposed angular velocity with a mean error of around -10 deg s^{-1} that was maintained constant throughout the duration of the presentation for both clockwise and counterclockwise rotations, indicating flies experienced a small, but measurable, amount of retinal slip during these periods. The error was calculated as the difference between the angular velocity of the fly and that of the visual scene.

To identify the control architecture that best predicted the behavior of the flies, I first presented a rotatory bias to the fly and then immediately turned off the LEDs in the arena, thus removing all visual feedback and subjecting the fly to an open-loop configuration. It is important to note that in our magnotether setup the fly is in closed-loop conditions whenever a visual scene is present because it is free to actively rotate; thus, closed-loop conditions are most easily created by simply turning off the visual display. To test if the flies' OMR persists following the visual presentation, I presented flies with alternating periods of closed-loop (LEDs on) and open-loop (LEDs off) conditions. During the closed-loop periods, I exposed flies to either a static scene or rotational motion (Figure 2.3C). As in the previous experiment, flies matched their own angular velocity to that of the visual scene. When the visual stimulus was turned off, flies maintained, on average, the angular velocity elicited by the preceding visual stimulus (either static or moving) (Figure 2.3E). I refer to this maintenance of locomotory bias after the visual stimulus has stopped, as the post-stimulus response (PSR) At the onset of the dark, open-loop periods, I observed a fast change in angular velocity, which I attribute to a startle response due to the large, rapid change in light intensity. Once this transient startle response subsided, flies roughly maintained the previously elicited angular velocity during both clockwise and counterclockwise rotations. Following the periods of darkness, flies quickly adjusted their angular velocity to that of the visual scene, with a time constant (~1 s) consistent with my previous experiments (Figure 2.3D). This result indicates that flies maintain their PSR for many seconds, but they quickly update their motor output once they experience closed-loop visual input again. As argued more fully below, these experiments indicate that the OMR exhibits features consistent with a PI controller.

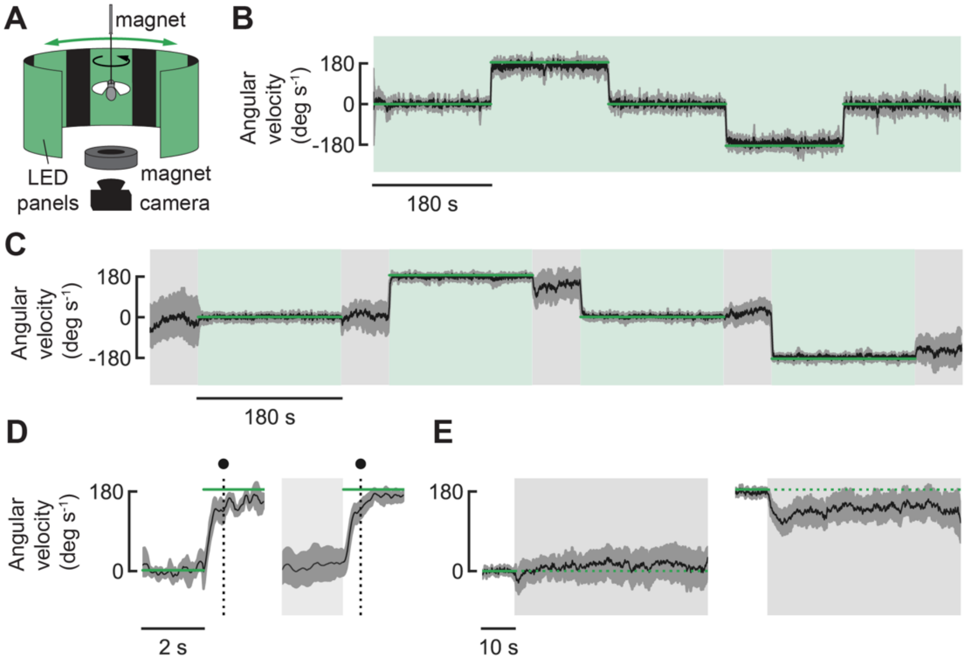

Figure 2.3: Flies maintain their optomotor response in the absence of visual stimuli.

(A) Schematic of the magnotether flight arena, which allows the fly to rotate in yaw (black arrow). The fly is centered in a curved visual display of green LEDs used to present visual stimuli, while the fly's body angle is tracked in real time using machine vision.

(B) Mean angular velocity during closed-loop presentations (green background) of alternating periods of a static and rotating visual scene. The green lines indicate the angular velocity of the visual scene. The solid dark line is the mean of all individuals (n=10), and the grey shaded area is the bootstrapped 95% CI for the mean. During periods of rotating visual motion, the visual scene was rotated at 184.6 deg s^{-1}.

(C) Mean fly angular velocity during intercalated periods of open and closed loop. During open-loop periods (gray background), the fly was left to fly in complete darkness, with no visual feedback. The solid dark line is the mean of all individuals (n=30), and the grey shaded area is the bootstrapped 95% CI for the mean.
(D) On the left, mean angular velocity during transitions between a static and a rotating visual scene. The mean is averaged over all the transitions from static to rotating scene in (B). The traces were normalized to be plotted as a clockwise rotation. On the right, mean angular velocity during transitions between a dark period and a rotating visual scene. The mean is averaged over all the transitions from dark periods to a rotating scene in (C). The black dotted line indicates the mean time it took for flies to match the 95% of the angular velocity of the visual scene.
(E) On the left, mean angular velocity during transitions between a static and a dark period. The mean is averaged over all the transitions from a static to dark periods on (C). On the right, mean angular velocity during transitions between a period of a rotating visual scene and darkness. The mean is averaged over all the transitions from rotating scenes to dark periods on (C). The traces were normalized to be plotted as a clockwise rotation.

To investigate if the PSR is in part influenced by saccades, I identified large and rapid changes in angular velocity for all flies in the experiment shown in Figure 2.3C (Figure 2.4). I found no significant bias in the directionality of saccades during the open-loop periods, suggesting saccades do not play a major role in the maintenance of the PSR. I did observe a small increase in saccade rate for saccades that were in the direction of rotation during periods of visual motion, but this trend is not significant. The rate of saccades during the dark, open-loop periods seemed to reflect the rate during the preceding visual stimulus period; saccade rates were lower during dark periods that followed a static scene compared to those following a rotating scene. The saccade rate during static scenes was also significantly lower ($p<0.05$) than that during a rotating scene.

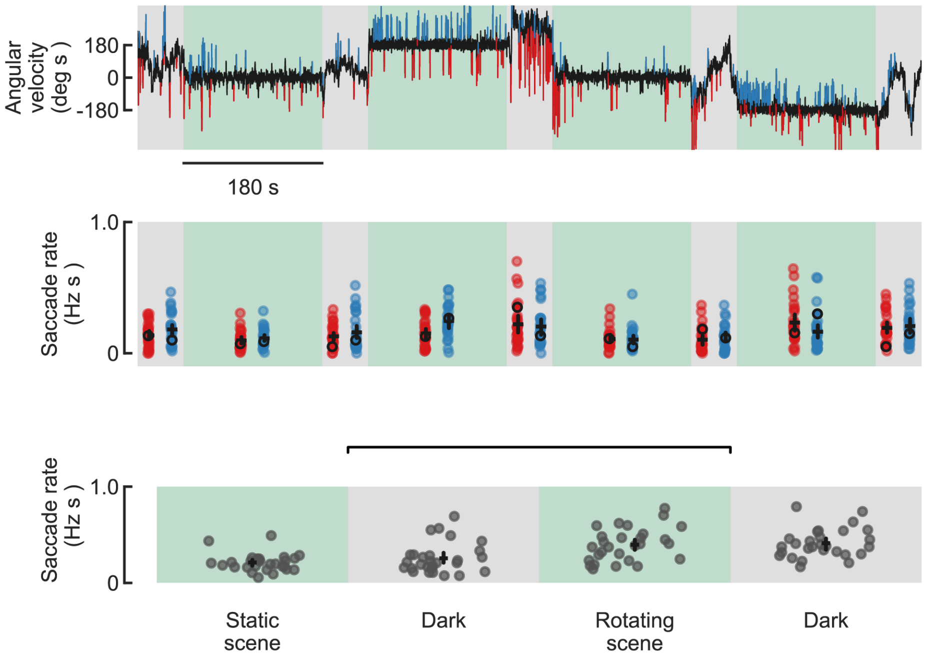

Figure 2.4: Saccade detection during the periods of open and closed-loop.

(A) Example angular velocity trace showing the detected saccades from an individual in the experiment shown in Figure 2.4C, saccades to the left are plotted in red, and saccades to the right are shown in blue.

(B) Saccade rate per second for each period for all individuals. Each dot represents an individual, the dot outlined in black shows the saccade rate for the trace shown in A. The mean across individuals is shown as a horizontal line, and the vertical lines indicate the 95% CI.

(C) Saccade rates during periods of static and rotating scene and the subsequent dark period. I combined data from both clockwise and counterclockwise rotations and the following dark periods, along with data from static scenes and their subsequent dark periods. I performed a Tukey's HSD pairwise group comparison across the four groups to determine statistical significance. All groups were statistically different from each other, with the exceptions being between the static scene and its following dark period, and between the rotating scene and its subsequent dark period.

Flies maintain their PSR with higher fidelity following longer optomotor stimulations

To test how long flies can maintain the locomotory bias after the cessation of the visual stimulus, I exposed flies to a period of rotational bias under closed-loop followed by a long, dark, open-loop period of 15 min. In each trial, I subjected the fly to a 3-min dark period, during which I tracked its angular velocity in real time to measure the inherent locomotory bias of each individual prior to any experience with the rotational bias. I then presented 3 min of rotational motion, where the scene was rotated in the opposite direction from the rotation each fly held during the initial dark period, to deliberately set the imposed bias in the opposite direction of the fly's initial intrinsic bias. I then removed the visual stimulus and tracked the fly's angular velocity for 15 min in the dark (Figure 2.5A). Traces were normalized to be plotted as a counterclockwise turn. During the initial dark period, flies rotated at different angular velocities, but once the visual stimulus was presented, they matched the angular velocity of the rotating scene. During the following 15-min, dark period, flies maintained the PSR for several minutes. Although the flies' PSR did slowly drift toward zero over time, but the results indicate a very long maintenance of the PSR following the offset of the visual stimulus.

To study how the magnitude of the PSR was influenced by the duration of the prior visual bias presentation, I exposed flies to an array of different stimulus periods (3, 10, 30, 40, 60, 80, 90, 100, and 180 s) in either the clockwise or counterclockwise direction, followed by a 60 s dark period (Figure 2.5B, right column). I chose direction of rotation of the step stimulus at random, and included an initial control period in which I did not rotate the scene (Figure 2.5B, left column). The step change in the angular velocity of the visual scene simulates a sudden perturbation for which the fly must compensate, so I refer to the rotational period as a closed-loop bias, the length of which I systematically varied. Even bias durations as brief as 3 seconds resulted in a sustained PSR. However, the angular velocity during darkness decayed faster after short bias durations, and was maintained with higher fidelity following longer bias durations (Figure 2.5C, D). In all the traces following the step stimulus, I observed an immediate, fast drop in angular velocity once the dark period began, which I attribute to a startle response due to the rapid drop in light intensity from the LED screen. However, the duration of this putative startle response was temporary, as opposed to the PSR, as evidenced by the responses to bias durations lasting longer than about 30 seconds (Fig. 2.5C).

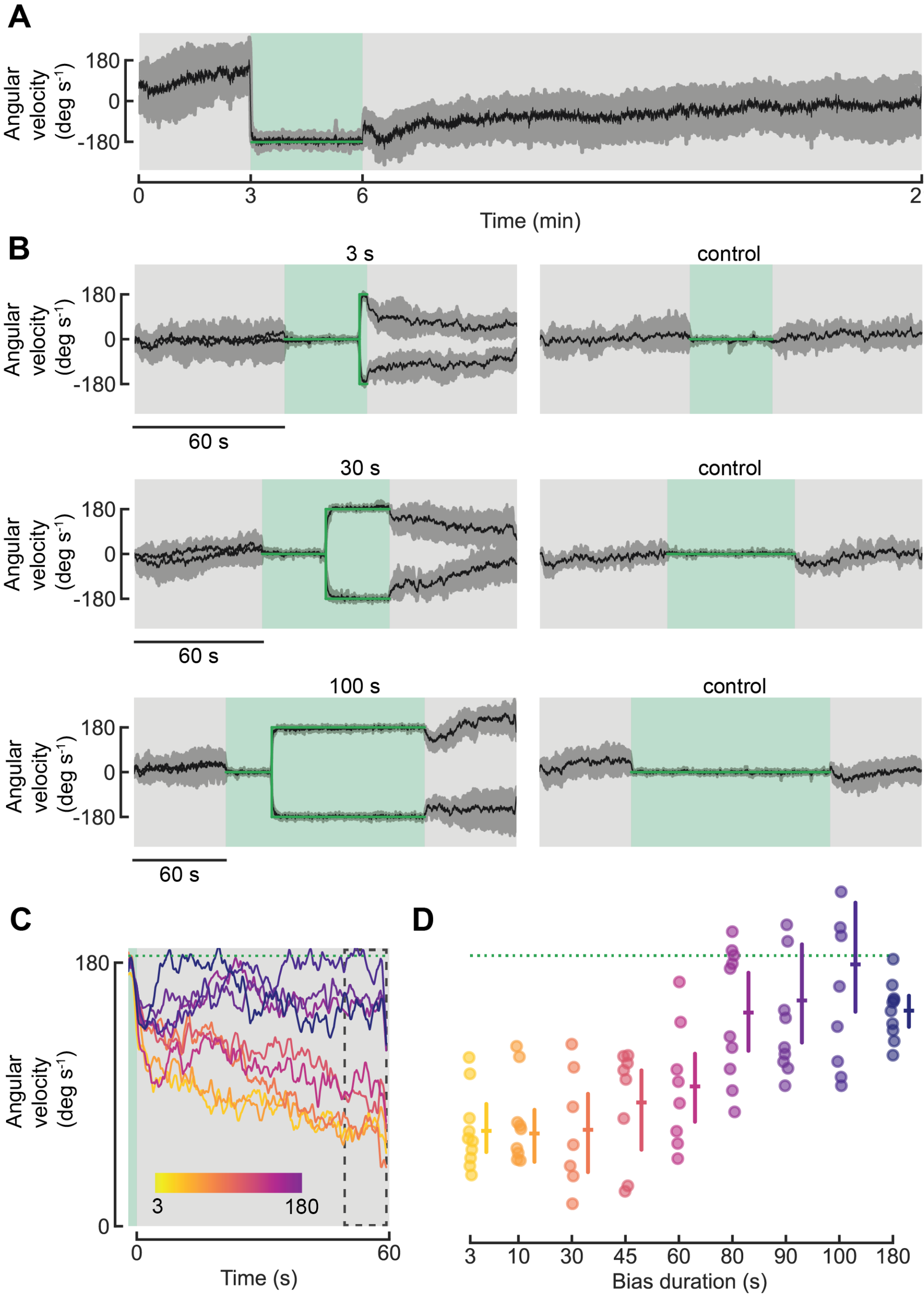

Figure 2.5: Flies maintain their optomotor response with higher fidelity following longer optomotor stimulations.

(A) Mean angular velocity during a sequence of 3 min dark period, 3 min rotating scene, followed by a 15 min dark period. During the first period of darkness, each fly's angular velocity was monitored in real time, the following rotating scene was moved in the opposite direction of the rotation each fly held during the initial dark period. The traces were normalized to be plotted as a counterclockwise rotation. The solid dark line is the mean of all individuals (n=10), and the grey shaded area is the bootstrapped 95% CI for the mean.

(B) Mean angular velocity during dark periods before and after a step stimulus varying the angular velocity of visual scene for different durations. On the right: solid dark lines are the mean of means of all clockwise (2 trials per individual) and counterclockwise (2 trials per individual) rotations trials for all individuals (n=10), and the gray shaded area is the bootstrapped 95% CI for the mean. Numbers on top of the dark green patch indicate the duration of the rotating visual stimulus. On the left: The control condition where the visual scene was not rotated but left static. The solid dark lines are the mean of means of all trials (4 trials per individual) for all individuals (n=10), and the gray shaded area is the bootstrapped 95% CI for the mean. The data for the experimental and control conditions come from the same individuals, but each duration tested was collected using a different set of flies.

(C) Mean angular velocity traces during dark periods following step stimuli varying the angular velocity of visual scene for different durations. The duration of the rotating stimulus, or bias duration, is indicated by the color of the trace, with the shortest duration plotted in yellow, and the longest in purple. The green patch shows the last 2 seconds of the optomotor stimulation, and the green dotted line indicates the angular velocity of rotating scene during the visual presentation. Each trace is the mean of means of all trials for all individuals (4 trials per individual, n=10), clockwise and counterclockwise rotations were normalized and averaged to obtain each trace. The black dotted rectangle indicates the last ten seconds of data used to plot data in (D).

(D) Mean angular velocities for all individuals during the last 10 s of a 60 s dark period (shown in a dotted rectangle in C) following different durations of optomotor stimulation, or bias. The colors correspond to the duration of the bias. The horizontal lines show the mean of all individuals, and the vertical lines show the 95% CI.

Characterization of the integrative features of the OMR using system identification

Although some prior research has focused on the integral gain component of the OMR (Schnell et al., 2014; Wolf and Heisenberg, 1990), the controller in flies has often been modeled as a proportional (P) controller because this simple configuration captures the behavior with reasonable accuracy. However, our open-loop behavioral experiments showing evidence of a PSR after visual feedback is removed—and its correlation with the duration of the prior visual stimulus—suggests that some process that resembles an integrative gain term element is likely present within the fly's OMR feedback control system. Thus, I used standard system identification principles to more fully characterize the integral gain component (Figure 2.6).

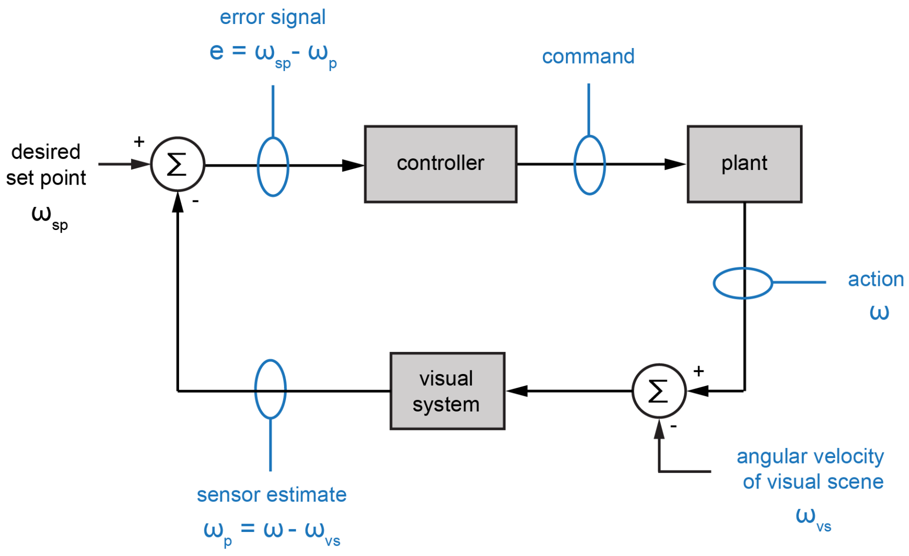

Figure 2.6: Our model of the feedback control loop for the yaw OMR with the system variables involved. The plant models the fly’s inertial dynamics and damping, and the resulting action is the fly’s angular velocity that I measure in our setup (ω). The visual system acts as the sensory input and measures the angular velocity of the surround perceived by the fly (ω_p), which is the angular velocity of the visual scene I present to the fly in our LED arena (ω_{vs}), subtracted from the fly’s own angular velocity. The ω_p is compared with a desired set point (ω_{sp}), to produce an error signal. The controller processes the error signal and sends commands to adjust the fly's motor actions, thus regulating its angular velocity in yaw to align with the visual environment.

I modeled the dynamics of a simple yaw velocity controller with the following equation:

$$I\omega' = -C\omega + U(t, \omega), \qquad (2.1)$$

where I and ω' are the fly's inertia and angular acceleration, respectively, C is the damping constant, and U is the controller's output. I first characterized the observed yaw dynamics of the fly only during closed-loop periods. To do this, I used the closed-loop experimental data shown in Figure 2.5B, where flies responded to step changes in angular velocity of the visual panorama for a range of durations. To obtain a single mean trace for each stimulus duration I combined the closed-loop yaw OMR responses into one trace per duration, assuming that the clockwise and counterclockwise rotations would evoke symmetrical behaviors. Initially, I modelled these closed-loop periods as a P controller, similar to the existing literature (Cellini et al., 2022), in which the fly's turning torque is proportional to the error e, representing the retinal slip it perceives. The output of the P controller is then given by:

$$U(t, \omega) = K_c\, e, \qquad (2.2)$$

where K_c is the fly's visuomotor gain and e is the error given by subtracting the angular velocity perceived by the fly (ω_p), from its desired set point (ω_{sp}) which in this case was set to zero. In our setup, ω_p calculated by subtracting the angular velocity of the fly (ω), from the angular velocity of the stimulus presented in our LED arena (ω_{vs}). The error can then be written as:

$$e = \omega_s - (\omega - \omega_{vs}). \qquad (2.3)$$

Equation 2.1 may then be rewritten as:

$$\omega' = -D\omega + K_p\ (\omega_{vs} - \omega), \qquad (2.4)$$

where D is the damping coefficient equal toa damping constant, C, divided by the flies' inertia, I (i.e. $D = C/I$), and K_p is the proportional gain, equal to (K_c/I). The solution to equation 2.4 during a closed-loop step change in ω_{vs}, as in our experiment shown in Figure 2.5B, is given by:

$$\omega(t)\ = \omega_{eqCL} + \left(\omega_0 - \omega_{eqCL}\right) exp^{-(D+K_p)t}, \qquad (2.5)$$

where ω_{eqCL} is the fly's angular velocity at equilibrium (i.e., when $\omega' = 0$). In the case of our step stimulus, this condition is reached when the fly in maintaining a stable angular velocity approximately matching the rotating surround. This solution assumes the step stimulus starts at t=0, and that ω_{vs} is held constant throughout the stimulus duration. Given those conditions, ω_{eq} is equal to:

$$\omega_{eqCL}\ = \frac{K_p\ \omega_{vs}}{K_p + D}. \qquad (2.6)$$

I then used non-linear least squares fit on equation 2.5 to determine the proportional gain (K_p), and the damping coefficient (D), for each of the mean closed-loop traces corresponding to the different bias durations presented. I performed the fits on each of these traces individually, and thus obtained a K_p and D value for each of the stimulus durations (Figure 2.7), all the estimated parameters from this analysis are shown in Table 2.1.

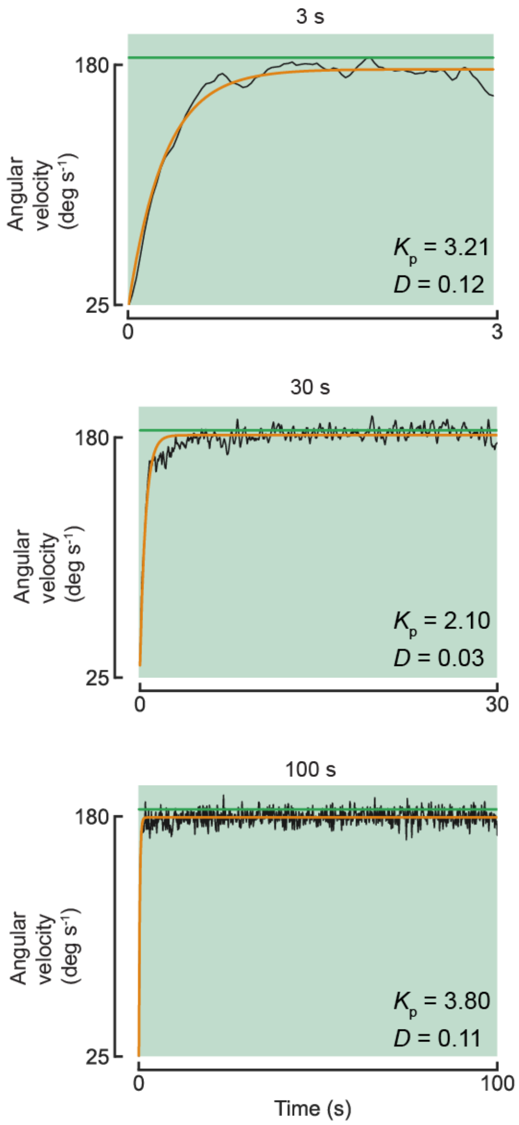

Figure 2.7: P controller fits and angular velocity traces during closed-loop period.

P controller fits, along with the estimated K_p, D coefficients for the 3-s, 30-s, and 100-s closed-loop step stimulus durations. The solid back line is the mean angular velocity trace, the fits are shown in orange, and the angular velocity of the visual scene (ω_{vs}) is plotted as a green line. To ensure all traces are aligned at the same starting point, the fit was calculated from the moment the angular velocity trace was higher than 25 deg s^{-1}. The average goodness of the fit (R^2) was 96 % ± 3.

Bias duration	**Estimated K_p**	**Estimated D**
3 s	3.21	0.12
10 s	3.47	0.11
30 s	2.10	0.03
40 s	3.38	0.13
60 s	3.54	0.16
80 s	3.08	0.10
90 s	3.42	0.03
100 s	3.80	0.11
180 s	4.79	0.14

Table 2.1: Estimated proportional gain, and damping coefficient.

Proportional gain, *Kp*, and damping coefficient, *D*, estimated from the mean trace of the different durations of angular velocity step stimuli.

The estimated values of K_p, and D are consistent with those reported in previous studies (Salem et al., 2022; Salem et al., 2023), and the high goodness of fits (R^2 = ~96%) confirm that a P controller can accurately capture the behavior observed during closed-loop periods. Note that the mean angular velocity traces and their corresponding fits do not exactly reach the angular velocity of the rotating surround; rather they remain approximately ~10 deg s^{-1} below the angular velocity of the rotatory bias. This is an expected feature of a P controller because this architecture can minimize, but not completely eliminate, the steady-state error. However, the P controller should also provide a clear prediction of what the behavior once the feedback loop is opened, in this case, when I turn off the arena LEDs. Assuming that in open loop the error becomes zero (because the fly is in the dark and no longer can estimate of the angular velocity of the surround), I can calculate the fly's expected angular velocity using equation 2.4, in which the proportional term becomes zero, and may be written as:

$$\omega' = -D\omega, \text{ and} \qquad (2.7)$$

$$\omega(t) = \omega_f \, exp^{-t/\tau}, \tag{2.8}$$

where τ is the decay constant equal to (1/*D*), and ω_f is the fly's angular velocity at the end of the closed-loop epoch, just before the feedback loop is opened. From equation 2.8 is evident that the once the visual stimulus is removed, the angular velocity should decay depending entirely on the damping coefficient. Using our estimated *D* values in Table 2.1, I can plot the angular velocity traces predicted from the P controller model during the dark period (Figure 2.8).

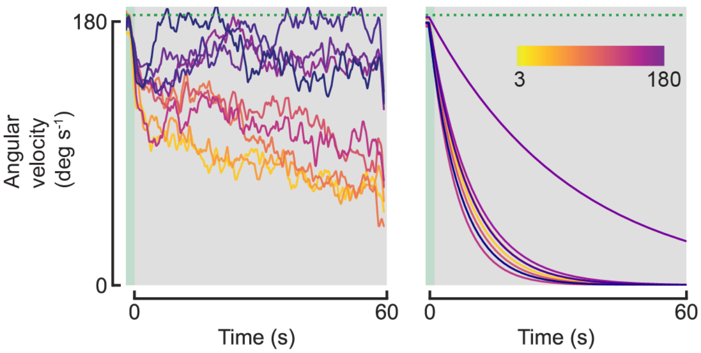

Figure 2.8: P controller predicted angular velocity traces during the dark period.

On the left: Experimental data, same plot as in Figure 2.5C.

On the right: P controller predicted angular velocity traces during the dark period following step stimuli varying the angular velocity of the visual scene for different durations. The duration of the rotating stimulus, or bias duration, is indicated by the color of the trace, with the shortest duration plotted in yellow, and the longest in purple. The green patch shows the last 2 seconds of the optomotor stimulation, and the green dotted line indicates the angular velocity of the rotating scene during the visual presentation.

The estimated damping coefficients for the 3-s and 90-s bias durations (Table 2.1) are significantly lower than those estimated for other bias durations, resulting in a slower decay of angular velocity during the dark period. However, all other predicted traces decay to zero much faster than observed in our experimental data (Figure 2.5C). Also, the P controller does not predict different decay constants depending on the bias duration, in contradiction to the clear trend in our experimental data. Altogether, our behavioral experiments suggest that an integrative gain term is necessary in the model of the feedback loop to model the fly's behavior more accurately.

Estimation of the integral gain

The output of a PI controller is described by the equation:

$$U(t, \omega) = K_p\, e + K_i \int_0^f e\, dt, \tag{2.9}$$

where K_p is the proportional gain and e is the error as mentioned above, but K_i is the integral gain. Equation 2.9 assumes the rotating stimulus starts at t=0, and ends at t=f, therefore the temporal integral of the error during the closed-loop period is multiplied by K_i to get the integral component of the controller's output. Substituting the output of the PI controller in equation 2.1, which describes our feedback control loop, results in the following equation:

$$\omega' = -D\omega + K_p\,(\omega_{vs} - \omega) + K_i \int_0^{tf} (\omega_{vs} - \omega) dt. \tag{2.10}$$

Assuming the error becomes zero once the feedback loop is opened, the fly's angular velocity in the dark period would depend on the damping coefficient plus the integral term as follows:

$$\omega' = -D\omega + K_i\, \eta_f \text{ , where} \tag{2.11}$$

$$\eta_f = \int_0^{tf} (\omega_{vs} - \omega) dt. \tag{2.12}$$

From our closed-loop experimental data, I can compute the integral of the error (η_f) and use equation 2.11 to solve e for ω_{eqOL}, the fly's angular velocity at equilibrium (ω_{eqOL}):

$$\omega_{eqOL} = \frac{K_i \, \eta_f}{D} \cdot \tag{2.13}$$

It is important to note that ω_{eqOL} is obtained from the experimental open-loop data, and is different from the ω_{eqCL} calculated above for the P controller model using closed-loop data.

To then evaluate the angular velocity at any time, t, during the open-loop period, I use equation 2.11 as follows:

$$\omega(t) = \omega_{eqOL} + \left(\omega_0 - \omega_{eqOL}\right) \, exp^{-D \, \Delta t}, \tag{2.14}$$

where ω_0 is the angular velocity at the start of the open-loop period at t_0, and Δt is the duration of the open-loop period, in this case, 60 s.

Solving then equation 2.14 by replacing ω_{eqOL}, the integral gain can be calculated as follows:

$$K_i = \frac{D}{\eta_f} \left[\frac{\omega(t_0 + \Delta t) - \omega_0 \, exp^{-D \, \Delta t}}{1 - \, exp^{-D \, \Delta t}} \right] \tag{2.15}$$

In summary, to empirically estimate the magnitude of integral gain term, I computed the integral of the error during closed-loop periods for each bias duration, and determined the integral gain, K_i, using equation 2.15 (Figure 2.9 and Table 2.2). Overall, the estimated integral gains were small, and broadly consistent across the different bias durations, suggesting that a small gain is enough to explain the long maintenance of the angular velocity during the dark period.

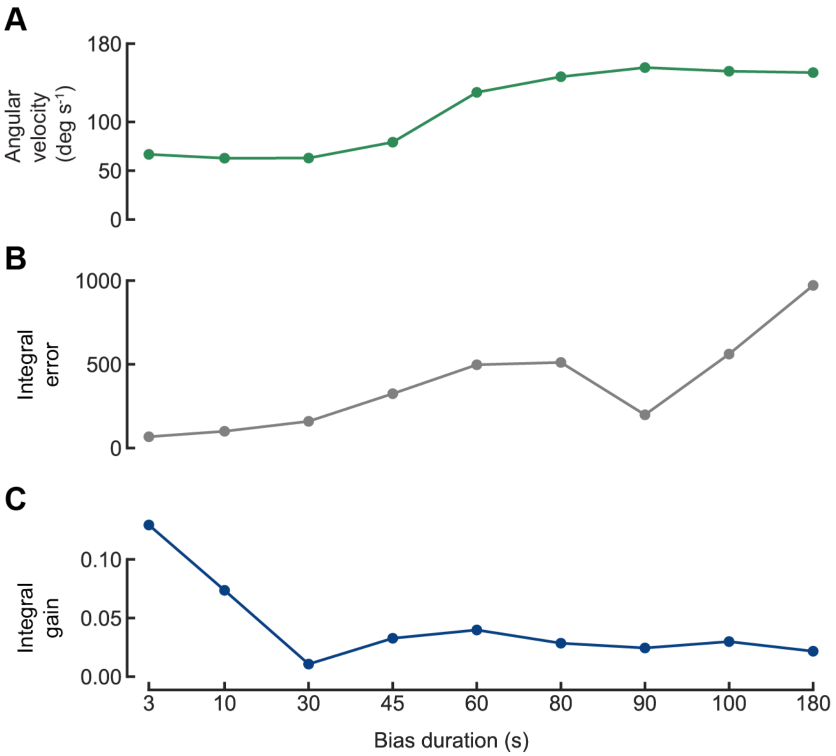

Figure 2.9: Empirically estimated integral gain for each of the bias durations.

(A) Calculated angular velocity at the end of the dark period following different durations of rotating stimulus, or bias durations.

(B) Integral of the error during closed-loop periods of rotational motion of different durations.

(C) Calculated integral gains for the different bias durations.

Bias duration	**Estimated K_i**
3 s	0.13
10 s	0.07
30 s	0.01
40 s	0.03
60 s	0.04
80 s	0.03
90 s	0.02
100 s	0.03
180 s	0.02

Table 2.2: Empirically estimated integral gain for each of the bias durations.
Values shown in Figure 2.9C.

Our previous estimates of proportional gain, damping, and integral gain are very similar across the different bias durations, suggesting a single controller can explain the observed behavior. Therefore, I performed a non-linear least squares fit on both the open and closed-loop periods using all the traces corresponding to the different bias durations to obtain a single ensemble fit. For this, I found the best fit across all the bias duration traces, rather than fitting each one individually. I performed the non-linear least squares fit on equation 2.5 and 2.14 for the closed and open-loop, respectively. The values I obtained from this ensemble fit, that includes all the traces for all the different bias durations, are listed in Table 2.3, and the integral gain is consistent with the ones I estimated algebraically for each bias durations separately (Table 2.2).

	K_p	D	K_i
Ensemble fit of all bias durations	3.08	0.07	0.04

Table 2.3: Proportional gain, damping, and integral gain obtained from fitting a PI-controller model on all the bias duration traces.

Values obtained from the ensemble fit.

Using the damping, proportional, and integral gain values obtained from the ensemble fit, I then plotted the angular velocity traces predicted from the PI controller model during the dark period for the different bias durations (Figure 2.10). The implementation of this small integral value was enough to recapitulate several aspects of the behavior observed during the open-loop period. The PI controller model correctly predicted the maintenance of the angular velocity for all bias durations, and also recapitulated the observed correlation between bias duration and decay constant.

To assess if the addition of this integral term improves the fit during the closed-loop periods, when the fly is actively controlling its yaw angular velocity, I calculated the output of the PI model during the imposed step change in rotational velocity (Figure 2.11). The addition of the integral term resulted in a very similar fit to the data as the P controller (R^2: ~93%). Although a small integral term is enough to explain the open-loop data, it did not improve the fit during closed-loop periods. This suggests that the effect of a very small integrator term in the control of yaw angular velocity is not evident in the compensation of an imposed bias as measured in this experiment.

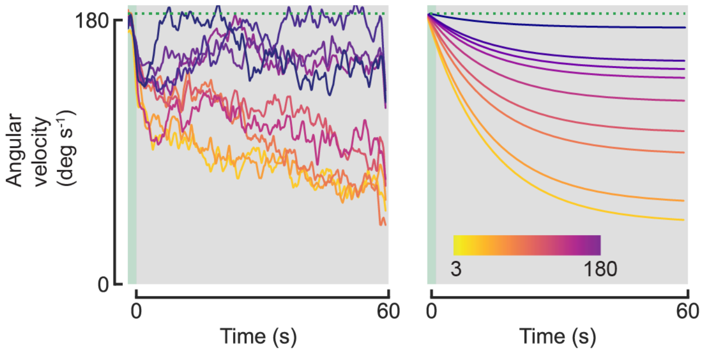

Figure 2.10: PI controller predicted angular velocity traces during the dark period.

On the left: Experimental data, same plot as in Figure 2.5C.

On the right: Pi controller predicted angular velocity traces during the dark period following step stimuli varying the angular velocity of visual scene for different durations. The duration of the rotating stimulus, or bias duration, is indicated by the color of the trace, with the shortest duration plotted in yellow, and the longest in purple. The green patch shows the last 2 seconds of the optomotor stimulation, and the green dotted line indicates the angular velocity of rotating scene during the visual presentation.

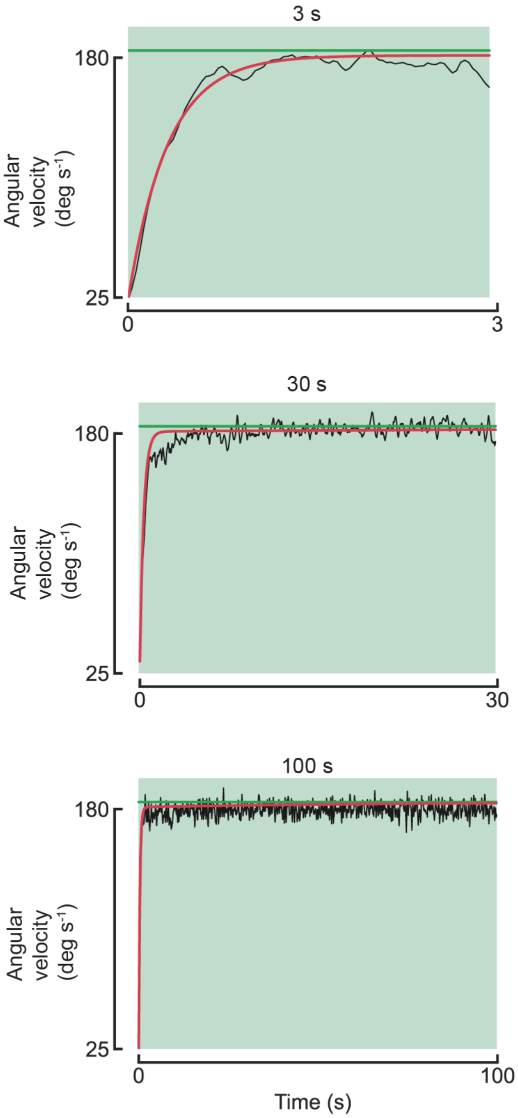

Figure 2.11: PI controller fits and angular velocity traces during closed-loop period.

PI controller fits for the 3-s, 30-s, and 100-s closed-loop step stimulus durations. The solid back line is the mean angular velocity trace, the fits are shown in orange, and the angular velocity of the visual scene (ω_{vs}) is plotted as a green line. To ensure all traces are aligned at the same starting point, the fit was calculated from the moment the angular velocity trace was higher than 25 deg s^{-1}. The average goodness of the fit (R^2) was 93 % ± 5.

Potential functional advantage of an integral gain in the control of yaw angular velocity

Our results suggest the fly's yaw OMR can be best approximated using a PI controller model. This model recapitulates the flies' motor output during closed-loop periods, as well as the PSR observed during open-loop periods. However, during closed-loop periods, our results show that a P controller, a simpler control architecture, is sufficient to explain the fly's responses. It is then unclear how a PI controller could be used in non-laboratory conditions, where flies have access to constant access to visual feedback.

How optic flow is detected by the fly's visual system, and how the neural circuits process these signals has been intensely studied in laboratory experiments (Ryu et al., 2022). In nature, as flies navigate complex environments, they rely on their visual system to provide estimates of their velocity with respect to the environment from optic flow (Krapp and Hengstenberg, 1996; Krapp et al., 1998). Laboratory experiments have shown flies lose spatiotemporal visual abilities as light levels drop (Palavalli-Nettimi and Theobald, 2020). Thus, under dim light conditions, the fly may lose an accurate estimate of its angular velocity. For instance, a fly navigating in a landscape where the light intensity suddenly reduces (e.g. cloudy day) may go through patches where it effectively loses visual feedback. To investigate this scenario, I simulated the impact of transient feedback loss on the angular velocity of a fly (Figure 2.12). Specifically, I modeled how the loss of visual feedback for brief (5 s) periods affects the control of angular velocity in yaw using both a P and PI controllers.

For this simulation, I used the previously estimated values for damping, proportional, and integral gain shown in Table 2.3. I plotted the visual feedback on a scale from zero to one, zero corresponding to moments where the fly would be operating without visual feedback, or open-loop. I then calculated the angular velocity of the fly during a 1000 s period using a P, and a PI controller. This simulation assumed the fly has an existing intrinsic bias that, without correction, would result in a 30 deg s^{-1} error; thus, the fly would not be able to stabilize the scene. The angular velocity obtained using a P controller rapidly increased during the brief periods where the visual feedback was zero. During the 5-s open-loop periods, the fly's angular velocity quickly increased to ~7 deg s^{-1}; thus, during these moments, the fly would not be able to stabilize the scene. Conversely, the angular velocity trace calculated using a PI controller shows only a small (<1 deg s^{-1}) increase in angular velocity during the first period of simulated loss of visual feedback. During the rest of the simulated open-loop periods, the fly's angular velocity remains at 0 deg s^{-1}, showing the fly can effectively stabilize the visual scene, even in the absence of any visual cues.

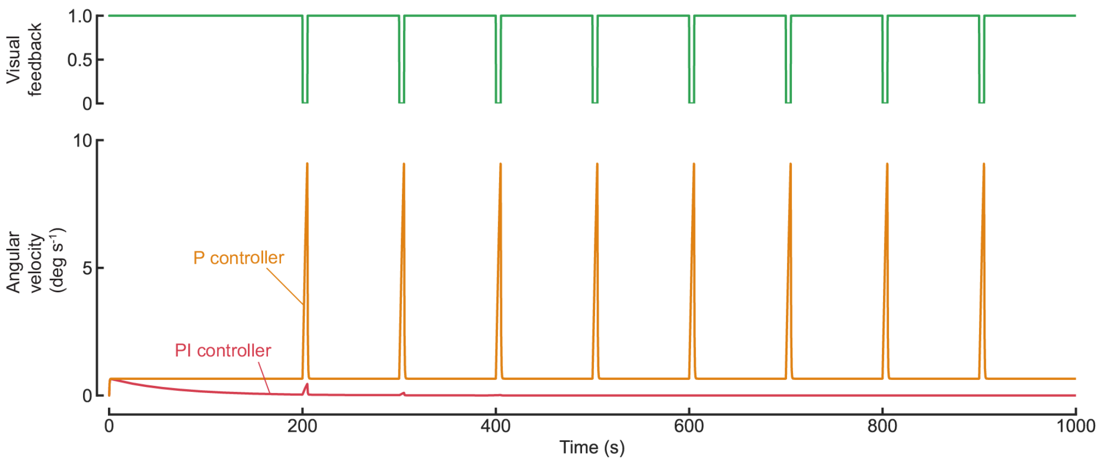

Figure 2.12: Simulation of the effect of intermittent loss of visual feedback on a fly's angular velocity controller by a P versus a PI controller.

Top panel shows the visual feedback, a value of 0 indicates the fly has no visual feedback and thus is operating in open-loop conditions.

Bottom panel: The angular velocity traces calculated using a P, and a PI controller. The P controller is plotted in orange, and the PI controller in red.

To further exemplify the effect of this small integral gain on the yaw angular velocity control, I simulated the resulting trajectory in 2D coordinates using the same parameters as in the simulation shown in Figure 2.12. I assumed a conservative groundspeed of 0.1 m s^{-1}. The resulting trajectory using a PI controller shows a fly would move in an approximately straight line for about 70 m, while the trajectory simulated using a P controller would result in almost circular trajectory of around 10 m in diameter.

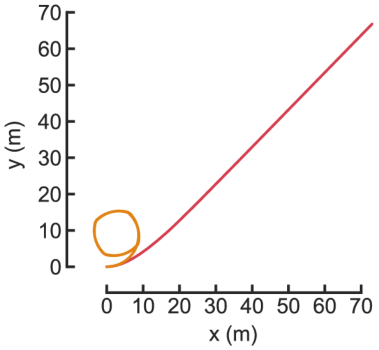

Figure 2.13: Simulation of the effect of intermittent loss of visual feedback on a fly's trajectory using a P versus a PI controller.

The trajectory calculated using a P controller for the fly's yaw angular velocity is plotted in orange, and the trajectory calculated using a PI controller is plotted in red.

2.4 Discussion

The OMR response is a well-studied reflex in *Drosophila* neurobiology, and while the integrative characteristics of the response have been noted in previous studies (Schnell et al., 2014; Wolf and Heisenberg, 1990), the size and effect of this integral gain has not been fully characterized. In this chapter, I showed the flies' yaw OMR can be best described by a PI controller. This model recapitulates the flies' motor output during the presentation of a rotating scene, as well as the maintenance of the elicited locomotory bias observed during the open-loop period, after the visual motion has ceased. Open-loop paradigms are commonly used in system identification because they make it possible to measure the controller output, without it influencing the input, as it would in an intact closed-loop system. In this case, the open-loop periods revealed an integrative process in the OMR, and allowed me to estimate the value of the integral gain.

While the flies' responses during the open-loop periods clearly showed that a P controller was insufficient to explain the behavior observed (Figure 2.8), the responses during closed-loop periods could be accurately modeled using P controller (Figure 2.7). This result is consistent with previous studies (Salem et al., 2022; Salem et al., 2023) that have modeled the control of yaw angular velocity using a P controller during closed-loop periods. This result raises the question of what the function of this integrative element is in controlling angular velocity, given flies typically operate in closed-loop conditions rather than the artificial open-loop periods used in these experiments.

However, flies navigate complex and diverse visual environments that can vary greatly in light intensity, contrast, etc. While the flies' visual system has been shown to quickly adapt to contrast changes (Matulis et al., 2020), at low light levels (lower than twilight level), flies have reduced spatio-temporal visual abilities (Palavalli-Nettimi and Theobald, 2020). Thus, in certain conditions, the fly might effectively be flying without an accurate estimate of the angular velocity of the visual scene. I hypothesize that under these conditions, the effect of even a small integral gain, might be crucial for the fly to maintain stable flight. To illustrate this, I performed a simulation where the fly loses visual feedback during short periods (Figure 2.12 and Figure 2.13), and found an integrative element was necessary for the fly to maintain stable flight.

While my experimental data are consistent with a PI controller in the OMR feedback control loop, further work is needed to demonstrate if a small integral gain is being used in the control of angular velocity. While my simulations show a clear advantage of the PI controller in the control of yaw angular velocity, it is unclear if flies ever experience open-loop conditions while navigating in natural environments.

2.5 Materials and methods

Flight arena

Behavioral experiments in the magnotether arena were performed by placing a tethered fly in the center of a circular (24 x 2 panels, 192 x 16 pixels) LED (470 nm) arena. The visual display was controlled using a panel controller (IORodeo) as described previously (Reiser and Dickinson, 2008). Flies were tethered to a magnetic pin and placed between two magnets, the top magnet has a jewel bearing (Microlap Technologies) glued on its bottom, which allows the fly to rotate freely in yaw with minimal friction. I used IR backlighting to illuminate the fly, and imaged from the bottom using a camera (FLIR, BFS-U3-16S2M-CS) at 30 fps. I tracked the fly's body orientation using a custom-written Python code in real time (https://github.com/willdickson/find_fly_angle). For all experiments, flies were placed in the arena and given at least 30 s to acclimate before starting the experiment. Flies that could not fly stably or at any point in the experiment rotated faster than 600 deg s^{-1} could not accurately be tracked and therefore excluded from the analysis. All the angular velocities traces were calculated using a Savitzky-Golay filter with a window length of 0.5 s, and a polynomial of order of 3.

Saccade Detection

The procedure to identify saccades from heading data has been previously described (Ros et al., 2024), and was used without modification.

Visual Stimuli

To investigate the persistent motor bias elicited by the presentation of a visual scene, I presented flies intercalated periods of closed- and open-loop. During closed-loop epochs, I presented either a static, or a rotating visual scene, and during open-loop epochs, I turned off all visual stimuli and let flies fly in complete darkness. For all magnotether experiments, I presented a rotating visual scene that consisted of uniformly spaced bars with a spatial wavelength of 30º rotating either clockwise or counterclockwise at a constant angular velocity of 184.6 deg s^{-1}. During static visual scene trials, I used this same stripped pattern, except for data shown in Fig. 1C, where I used a simulated sun (a single illuminated pixel) as a stationary visual cue.

Quantification and statistical analyses

Behavioral data were analyzed with custom software written in Python. Sample sizes refer to the number of individuals tested. Variance across individuals was quantified as the bootstrapped 95% confidence interval (CI), with 1000 bootstrapped iterations for the mean of the individual means.

System and parameter identification

The closed-loop parameter fit was done by using a non-linear squares fit to equation 2.1 using the 'BFG5' algorithm included in the python SciPy package. The open-loop parameter identification was performed using a custom software written in Python.

References

Bender, J. A. and Dickinson, M. H. (2006). Visual stimulation of saccades in magnetically tethered Drosophila. *Journal of Experimental Biology* **209**, 3170–3182.

Cellini, B., Salem, W. and Mongeau, J.-M. (2022). Complementary feedback control enables effective gaze stabilization in animals. *Proceedings of the National Academy of Sciences* **119**, e2121660119.

Chapman, J. W., Reynolds, D. R. and Wilson, K. (2015). Long-range seasonal migration in insects: mechanisms, evolutionary drivers and ecological consequences. *Ecology Letters* **18**, 287–302.

Dickinson, M. H. (1999). Haltere-mediated equilibrium reflexes of the fruit fly, Drosophila melanogaster. *Philos Trans R Soc Lond B Biol Sci* **354**, 903–916.

Dickinson, M. H. (2005). The Initiation and Control of Rapid Flight Maneuvers in Fruit Flies. *Integrative and Comparative Biology* **45**, 274–281.

Dickinson, M. H. and Muijres, F. T. (2016). The aerodynamics and control of free flight manoeuvres in Drosophila. *Philosophical Transactions of the Royal Society B: Biological Sciences* **371**, 20150388.

Ellington, C. P. and Lighthill, M. J. (1997). The Aerodynamics of Hovering Insect Flight. Vi. Lift and Power Requirements. *Philosophical Transactions of the Royal Society of London. B, Biological Sciences* **305**, 145–181.

Fuller, S. B., Straw, A. D., Peek, M. Y., Murray, R. M. and Dickinson, M. H. (2014). Flying Drosophila stabilize their vision-based velocity controller by sensing wind with their antennae. *Proceedings of the National Academy of Sciences* **111**, E1182–E1191.

Götz, K. G. (1968). Flight control in Drosophila by visual perception of motion. *Kybernetik* **4**, 199–208.

Götz, K. G. (1987). Course-Control, Metabolism and Wing Interference During Ultralong Tethered Flight in Drosophila Melanogaster. *Journal of Experimental Biology* **128**, 35–46.

Götz, K. G., Hengstenberg, B. and Biesinger, R. (1979). Optomotor control of wing beat and body posture in drosophila. *Biol. Cybernetics* **35**, 101–112.

Heisenberg, M. and Wolf, R. (1984). *Vision in Drosophila*. Berlin, Heidelberg: Springer.

Leitch, K. J., Ponce, F. V., Dickson, W. B., van Breugel, F. and Dickinson, M. H. (2021). The long-distance flight behavior of Drosophila supports an agent-based model for wind-assisted dispersal in insects. *Proceedings of the National Academy of Sciences* **118**, e2013342118.

Matulis, C. A., Chen, J., Gonzalez-Suarez, A. D., Behnia, R. and Clark, D. A. (2020). Heterogeneous Temporal Contrast Adaptation in *Drosophila* Direction-Selective Circuits. *Current Biology* **30**, 222-236.e6.

Möhl, B. (1988). Short-term learning during flight control inLocusta migratoria. *J. Comp. Physiol.* **163**, 803–812.

Mongeau, J.-M. and Frye, M. A. (2017). Drosophila Spatiotemporally Integrates Visual Signals to Control Saccades. *Current Biology* **27**, 2901-2914.e2.

Muijres, F. T., Iwasaki, N. A., Elzinga, M. J., Melis, J. M. and Dickinson, M. H. (2017). Flies compensate for unilateral wing damage through modular adjustments of wing and body kinematics. *Interface Focus* **7**, 20160103.

Palavalli-Nettimi, R. and Theobald, J. C. (2020). Small eyes in dim light: Implications to spatio-temporal visual abilities in *Drosophila melanogaster*. *Vision Research* **169**, 33–40.

Ristroph, L., Bergou, A. J., Ristroph, G., Coumes, K., Berman, G. J., Guckenheimer, J., Wang, Z. J. and Cohen, I. (2010). Discovering the flight autostabilizer of fruit flies by inducing aerial stumbles. *Proceedings of the National Academy of Sciences* **107**, 4820–4824.

Ros, I. G., Omoto, J. J. and Dickinson, M. H. (2024). Descending control and regulation of spontaneous flight turns in Drosophila. *Current Biology* **34**, 531-540.e5.

Salem, W., Cellini, B., Kabutz, H., Hari Prasad, H. K., Cheng, B., Jayaram, K. and Mongeau, J.-M. (2022). Flies trade off stability and performance via adaptive compensation to wing damage. *Science Advances* **8**, eabo0719.

Salem, W., Cellini, B., Jaworski, E. and Mongeau, J.-M. (2023). Flies adaptively control flight to compensate for added inertia. *Proceedings of the Royal Society B: Biological Sciences* **290**, 20231115.

Schnell, B., Weir, P. T., Roth, E., Fairhall, A. L. and Dickinson, M. H. (2014). Cellular mechanisms for integral feedback in visually guided behavior. *Proceedings of the National Academy of Sciences* **111**, 5700–5705.

Tammero, L. F. and Dickinson, M. H. (2002). Collision-avoidance and landing responses are mediated by separate pathways in the fruit fly, Drosophila melanogaster. *Journal of Experimental Biology* **205**, 2785–2798.

Tammero, L. F., Frye, M. A. and Dickinson, M. H. (2004). Spatial organization of visuomotor reflexes in Drosophila. *Journal of Experimental Biology* **207**, 113–122.

Wolf, R. and Heisenberg, M. (1990). Visual control of straight flight in Drosophila melanogaster. *J Comp Physiol A* **167**, 269–283.

Chapter 3

IMPLEMENTATION OF THE INTEGRAL GAIN IN THE FLIGHT MOTOR SYSTEM

3.1 Abstract

The optomotor response OMR is a robust reflex by which flies adjust their motor system to counteract locomotory biases from internal or external perturbations. In Chapter 2, I showed the behavior exhibited during the flies' yaw OMR is most accurately modeled by a PI controller. This model recapitulates the flies' motor output during the presentation of a rotating scene, as well as the maintenance of the elicited locomotory bias, or post-stimulus response (PSR), observed after the visual motion has ceased. In this chapter, I examine how the flight musculature may implement integral and proportional control. Using a previously described method, I imaged the activity of the steering muscles using a genetically encoded calcium indicator while measuring the wing stroke amplitudes of the wings in a rigidly tethered fly. To study the integrative characteristics of the OMR while imaging the activity of the steering muscles, I presented flies with a rotating visual scene and then stopped the visual motion to measure the locomotory bias elicited by the visual motion. Previous work has clarified that the fly's steering muscle system consists of two physiologically different groups of muscles: phasic and tonic. The activity of phasic muscles has been linked to large, transient changes in wing motion, while tonic muscles are specialized for continuous adjustments of wing motion. Therefore, I hypothesized that certain tonic muscles may be involved in the maintenance of the PSR. My results show that no single muscle is involved in the maintenance of the PSR, and rather, multiple muscles regulate wing stroke angle during the OMR and subsequent PSR. Further analysis showed that two tonic muscles are mainly involved in the regulation of wing stroke angle. These

results suggest that the integral implementation of the OMR is distributed among the fly's steering muscle system, particularly the tonic muscles.

3.2 Introduction

In Chapter II, I showed that a proportional-integral (PI) model best explains the behavior observed during flies' yaw optomotor response (OMR). This model recapitulates the flies' motor output during the presentation of a rotating scene, as well as the maintenance of this locomotor bias, or post-stimulus response (PSR), observed after the visual motion has ceased. Here, I investigate how flies control their musculature to generate the wing motion necessary for the OMR and the subsequent PSR; specifically, how a proportional and integral gain might be implemented within the flight motor system. As previously discussed, flying insects continuously update their motor actions based on sensory information to correct for aerodynamic instabilities and avoid collisions, predators, etc. The speed with which sensory signals are transformed into motor action is particularly impressive in flies, which can respond to a looming threat with a directed maneuver with ~50 ms. In addition to rapid changes in course, flies can also maintain a stable heading over long timescales, a deceptively simple feat that actually requires quite sophisticated adjustments of wing motion to continuously compensate for perturbations. This motor flexibility is possible due to specialized flight musculature, which has been extensively studied, enabling detailed analysis of how different control strategies are implemented in the flight motor system.

In most flying insects, including Diptera, the flight musculature consists of two functionally different kinds of muscle for power and steering (Heide, G., 1983). The power muscles (Figure 3.1) are a set of large, asynchronous muscles whose individual contractions do not correspond in a one-to-one fashion to motor neuron spikes but are rather activated mechanically by stretch (Josephson et al., 2000; Pringle, 1949). These muscles insert on the walls of the thorax in an approximately orthogonal arrangement, creating a self-oscillatory system that drives the back-and-forth motion of the wings (Pringle, 1957). Dorsal longitudinal muscles (DLMs) contract to move the wing forward while stretching and activating the dorso-ventral muscles (DVMs), which subsequently drive the wings backward while stretching the DLMs to continue the cycle. This stretch activation mechanism allows the wingbeat frequency to exceed the rate at which the nervous system can deliver impulses, facilitating the high wingbeat frequencies necessary for flight. This same stretch activation mechanism, however, makes the power muscles unsuitable for fine regulation of wing motion because they are only loosely controlled by the nervous system and are not directly attached to the base of the wing.

The more subtle changes in wing motion are controlled by the steering muscles (Figure 3.1), a set of 12 synchronous muscles that insert directly onto hardened cuticular elements of the exoskeleton known as sclerites, at the base of the wing. These muscles segregate anatomically into four major anatomical classes according to the sclerites on which they insert: the basalars (b1, b2, and b3), the first axillaries (i1 and i2), the third axillaries (iii1, iii3, and iii4), and the fourth axillaries (iv1, iv2, iv3, and iv4). Each steering muscle is innervated by one motor neuron (O'Sullivan et al., 2018; Trimarchi and Schneiderman, 1994), which means that the activity of just 24 motor neurons regulates wing motion. When considering the breadth of motor actions in the flies' behavioral repertoire, this is a relatively sparse control system.

Prior studies have shown how the steering muscles exert tension on each sclerite to modulate different aspects of wing motion (Lindsay et al., 2017; Melis et al., 2024). One way of regulating tension in this sparse system is adjusting the firing rate of each muscle. However, electrophysiological recordings have shown that flies can also adjust mechanical properties of muscles by regulating the firing phase within the stroke cycle (Tu and Dickinson, 1994). For example, a firing advance in the action potential of the motor neuron that innervates b1 can cause an increase in wing stroke amplitude, while a firing delay correlates with a decrease in stroke amplitude. Even though millisecond differences in the firing phase of motor neurons can affect the output of their target muscles on a stroke-to-stroke basis, a recent study (Melis et al., 2024) that recorded the activity in the steering muscles using a calcium indicator, was able to reconstruct the intricate pattern of wing motion with reasonable accuracy. Even though the steering muscles have different modalities to adjust tension on each sclerite, these changes may be correlated with certain features detectable by the imaging method. Thus, the muscle activity detectable via Ca^{2+} imaging is sufficient to reconstruct wing motion.

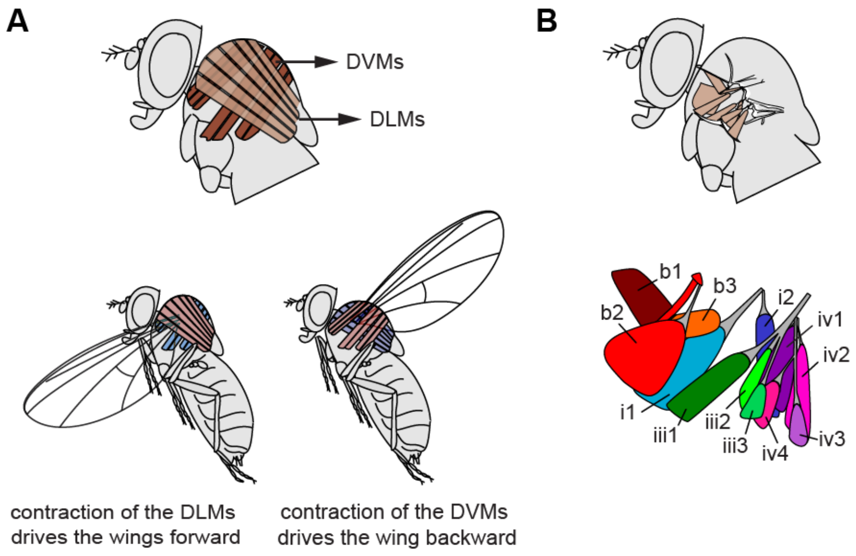

Figure 3.1: Schematic of the flight musculature.

(A) Schematic of the power muscles showing how they drive the back and ford motion of the wings. Figure reproduced from (Dickinson, 2006).

(B) Schematic of the steering muscles. The muscles segregate anatomically into four major groups according to the sclerites on which they insert. The basalars (b1, b2, and b3) are shown in red, the first axillaries (i1 and i2) in blue, the third axillaries (iii1, iii3, and iii4) in green, and the fourth axillaries (iv1, iv2, iv3, and iv4) in magenta.

The pattern of activity of the steering muscles can be categorized into two groups: phasic and tonic (Lindsay et al., 2017; Melis et al., 2024), although this stratification is not perfectly binary. Phasic muscles (b2, i1, iii1, iv1, iv3) are generally larger, quiescent, fire sporadically in bursts, and can generate large, transient changes in wing motion such as the ones needed during saccades. Tonic muscles (b1, b3, i2, iii3, iv4) are smaller, exhibit persistent patterns of activity, and are specialized for continuous adjustments such as the asymmetries in wing motion necessary for the OMR. Note that each anatomical class has at least one phasic and one tonic muscle. Recent work studying how flies regulate pitch angle, found that this stabilization behavior can also be modeled as a PI controller, and that the b1 and b2 muscles appear to implement the integral and proportional control features, respectively in the pitch rate controller (Whitehead et al., 2022). Therefore, I hypothesize that tonic and phasic muscles in the wing motor system might be similarly mapped onto the integral and proportional parameters for control in yaw. Using the same muscle imaging method used in previous studies, I explicitly examine which muscles are involved in the maintenance of the locomotor bias observed in the PSR, specifically, how the integral gain might be implemented.

In these experiments, I used an expanded version of the experimental set-up developed by Lindsay et al. 2017, which allows for simultaneous imaging of the steering muscles on both sides of the thorax while tracking the fly's wing stroke amplitude in response to visual stimuli (Figure 3.2A). I recorded the activity of the complete set of steering muscles using the genetically encoded calcium indicator, GCaMP7f, and used the previously described method to obtain the activity pattern of each steering muscle (Figure 3.2B).

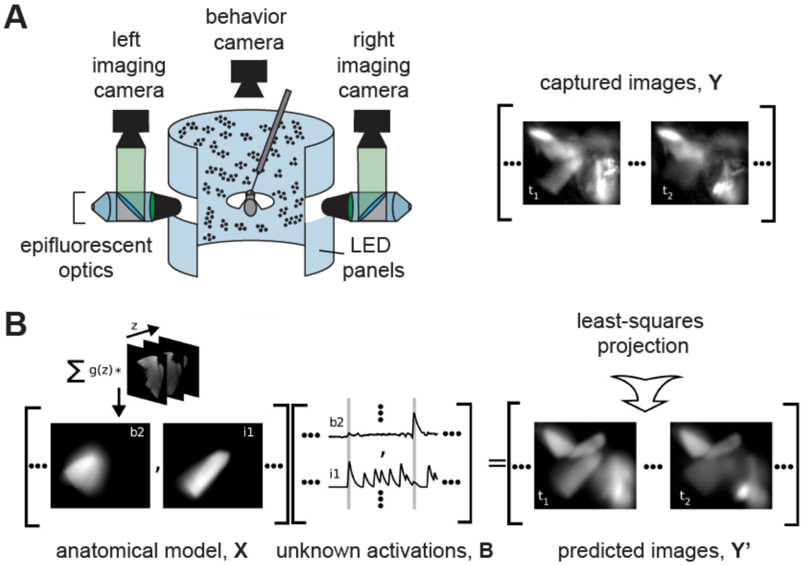

Figure 3.2: Muscle imaging experimental methods.

(A) Schematic of the muscle imaging flight arena (modified from (Lindsay et al., 2017). A fly is rigidly tethered in front of a curved visual display of green LEDs. The steering muscles on the left and right side of the fly are imaged using epifluorescent optics (see Methods for details). An image of the fly is captured and analyzed using a real-time machine vision system that measures the wingbeat amplitude of the wings.

(B) Analysis of the captured images to extract muscle activity traces as described in Lindsay et al., 2017. A z-stack of phalloidin-stained muscle images was used to generate a matrix of components, X, which predicts the spatial distribution of each muscle as captured by the imaging camera. The components corresponding to b2 and i1 are shown as an example. The muscle traces are solved for such that that X = Y', where Y' is the matrix of predicted images that minimized residual distance to the data in Y.

3.3 Results

The steering response elicited by an open-loop rotating visual stimulus outlasts the visual stimulus by many seconds

To study the integrative characteristics of the OMR in the muscle imaging arena, I performed experiments under open-loop conditions, in which the visual stimuli a fly experiences are decoupled from its motor actions. In an open-loop paradigm, I rotate the visual panorama around the fly at a constant speed and measure the difference in wing stroke amplitudes (WSA) of the two wings in a rigidly tethered fly, a signal that is known to be proportional to yaw torque (Tammero and Dickinson, 2002). This paradigm differs from the experimental conditions described in Chapter II, where I used a magnotether arena that allows flies to freely rotate in yaw. In thst setup flies have access to naturalistic sensory feedback from yaw rotation contributed by mechanosensory systems. However, prior work showed that the PSR can be induced by an open-loop visual stimulus in a rigid tether setup, like the one used here (Schnell et al., 2014).

To induce the OMR while imaging the activity of the steering muscles, I presented flies with a visual scene rotating at a constant angular velocity (30 deg s^{-1}) for 100 s, followed by the presentation of a static scene for 60 s (Figure 3.3). I normalized the responses to the direction of motion of the visual scene such that the WSA of the wing on the inside of the induced turn was subtracted from the WSA of the outside wing. This WSA differential (O-I) was used to quantify of the fly’s turning response. Upon presentation of the rotating scene, flies turned in the direction of motion as expected; the O-I WSA rapidly increased until it reached a plateau of ~20 deg that was maintained for the duration of the rotating scene. When the rotating scene stopped, flies maintained the turning response, or PSR, but the response decayed slowly over time. The time course of the PSR after a 100 s stimulus duration in this setup decays much faster than under closed-loop conditions in the magnotether apparatus, as described in Chapter II. However, the experimental conditions are not directly comparable because a rigidly tethered fly in the muscle imaging arena lacks mechanosensory feedback, and in this experiment an open-loop visual stimulus was used to induce the PSR.

During the presentation of the rotating scene, the outside and inside wing exhibited different time courses. At the onset of the rotating stimulus, the outside wing WSA rapidly increased by ~13 deg, but then decreased by ~7 deg after a few seconds (Figure 3.3B). In contrast, the WSA of the inside wing decreased at the onset of the stimulus and remains approximately constant. Thus, the sustained maintenance of the asymmetry in wing motion is mostly due to the action of the inside wing.

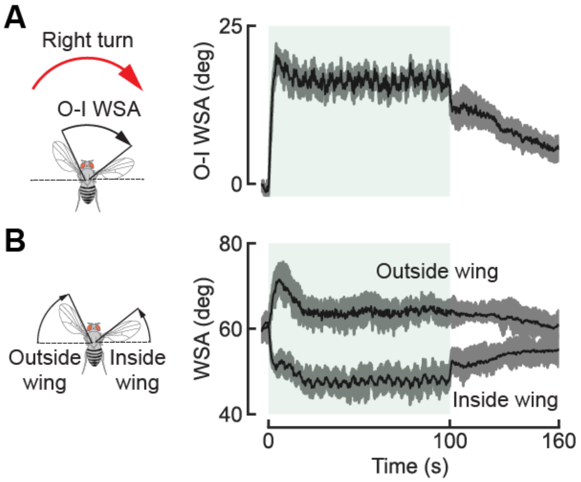

Figure 3.3: Behavioral responses during the presentation recorded in the muscle imaging arena.
(A) On the left, a schematic of the fly showing the measured wing stroke amplitude (WSA) differential. The WSA is normalized to the direction of motion of the visual scene such that the trace of the wing decreasing in amplitude (the inside wing, I), is subtracted from that of the wing increasing in amplitude (the outside wing, O). On the right, the outside minus inside wing stroke amplitude (O-I WSA) during a period of rotating visual scene (green patch), followed by a static visual scene period (white patch). The solid dark line is the mean of means for all individuals (n=34 individuals, 4 trials per fly), and the gray shaded area is the bootstrapped 95% CI for the mean.
(B) On the left, a schematic of the fly showing the measured wing stroke amplitudes of each wing. On the right, the traces corresponding to the outside and inside wings that results in the O-I WSA trace shown in (A). The

solid dark line is the mean of means for all individuals (n=34 individuals, 4 trials per fly), and the gray shaded area is the bootstrapped 95% CI for the mean.

Analysis of the WSA and muscle analysis traces

Lindsay and coworkers (Lindsay et al., 2017) showed that the activity of nearly all the steering muscles contribute to regulating the WSA, and that the continuous changes in WSA observed during the OMR are modulated by graded activity of the tonic muscles. However, the OMR stimulations used in their experiments were short (~3s) and thus it is unclear which muscles are responsible for maintaining the sustained asymmetries in response to much long stimulus presentation (~100 s) as shown in Fig. 3.3. The unmixing model described previously outputs fluorescence signals from the 12 steering muscles obtained from the images. Because the strength of fluorescence can differ per muscle and the exact lighting conditions can vary from fly to fly, it is necessary to scale the individual muscle activity traces. I normalized the raw fluorescence traces over the entire duration of the experiment by dividing each muscle trace by the standard deviation (S.D.) over the entire recording such that of 0 and 1 correspond to -2 and +2 S.D., respectively. I excluded from the analysis the b2 and iii1 muscles, because these phasic muscles are rarely active or are involved in motor actions that are not measured in these experiments. The iii1 muscle is rarely active during flight and its activity is correlated with wing folding, whereas b2 spikes correlate with very large fictive body saccades (see Lindsay et al., 2017, Figure 3), which were rare events in these recordings.

The behavioral data show a clear maintenance of the steering response after the rotating visual stimulus stopped. Nevertheless, responses vary among flies, with the locomotory bias potentially resulting from the outside wing maintaining a high WSA, the inside wing maintaining a low WSA, or both wings contributing to maintaining the turning response. This variation across flies and trials is quite typical when flies are operating in open-loop conditions (Tammero et al., 2004). To address this variability and because the steering muscles on each side of the thorax act independently on each wing, I analyzed the muscle activity of each wing separately. Additionally, when analyzing muscle activity during saccades, Lindsey and coworkers (Lindsay et al., 2017) observed that the activity of some muscles varies linearly with the WSA, but other muscles are only recruited for larger amplitude changes during saccades. To address if this pattern of recruitment also arises during the PSR, I analyzed the distribution of traces based on their mean amplitude during the 60 s period after the offset of the rotating stimulus. For the outside wing, trials in which the flies exhibited a low mean WSA (lower 25th percentile of the distribution) during the PSR were sorted into bin 1, trials in the middle of the distribution into bin 2, and trials that had a high WSA (upper 25th percentile) into bin 3. For the inside wing, I sorted trials with a high mean WSA (in the upper 25th percentile of the distribution) during the PSR into bin 1, those in the middle of the distribution into bin 2, and those with a low WSA (in the lowest 25th percentile) into bin 3. This sorting method places trials in which the WSA reflects the locomotor bias elicited by the preceding rotating scene into bin 3, while trials where the response decayed are placed into bin 1. I then calculated the mean WSA trace (Figure 3.4A), and the corresponding mean muscle traces for trials in each bin (Figure 3.4B).

Flies regulate WSA using multiple steering muscles during long OMR stimulations.

At the onset of the rotating stimulus, I observed changes in muscle activity in most of the muscles for both the outside and inside wing (Figure 3.4B). This is consistent with the previous literature (Lindsay et al., 2017) showing that WSA is modulated by multiple steering muscles. For example, the activity of iii3 is correlated with WSA for both the outside and inside wings, while the activity of b3 is negatively correlated. For the inside wing (which decreases in WSA), all fourth axillary muscles were recruited quite strongly, although the pattern of activity of iv3 that I observed was somewhat different from that reported by Lindsay et al., who found that the activity of iv3 was negatively correlated with changes in WSA, whereas I found that iv3 activity fell for both increases and decreases in WSA. However, one limitation of these muscle imaging studies is that the camera system for tracking wing motion only measures one kinematic angle (WSA), and thus other features of wing motion such as angle of attack or deviation from the stroke plane could be varying and correlated with the muscle activity observed.

While most muscles showed a large change of activity at the onset of the rotating stimulus, they exhibited different time courses of activity throughout the remainder of the presentation. This was mostly evident for the inside wing, which maintained a sustained decrease in WSA during the entire duration of the rotating stimulus. There are muscles that showed a rapid change at the onset of the stimulus such as b3 and iii3, but their activity then decreases, while others showed a sustained increase in activity such as i2, and iv2. It is important to note that while the mean traces of i1 and iv1 show a small, sustained increase in activity, the pattern of activity of these muscles is phasic, and thus are active in short bursts (Figure 3.5). Therefore, the small increase in activity exhibited by the mean traces of these muscles most likely comes from the averaging of many traces with interspersed bursts of activity. Because the trials were sorted according to their WSA during the PSR, and during the presentation of the rotating stimulus there are only small differences in WSA between the traces of each bin, the muscle activity traces of each of the data bins are virtually indistinguishable from each other.

Flies maintain the PSR using multiple steering muscles.

My data show that no single muscle exhibits persistent activity during the PSR, and thus multiple muscles are likely involved in maintaining the steering response (Figure 3.4B). To determine which muscles vary along with the WSA, I calculated the mean WSA for the traces of each of the data bins during the PSR (Figure 3.4C), as well as the corresponding mean muscle activity (Figure 3.4D).

For the outside wing, the difference in mean activity across the bins was very small for most muscles (Figure 3.4D, left column), suggesting small differences in activity across multiple muscles regulate the sustained increase in WSA. This is also evident from the muscle activity traces of each of the data bins (Figure 3.4B, left column), which show a very similar time course and intensity during the PSR. Whereas the differences in activity were small in most muscles, I did observe a significant change in the activity of i1, i2, iv1, and iv2 for trials in bin 1 (plotted in brown), which comprised trials where the PSR decayed. In this case, trials in which the WSA of the outside wing decreased during the PSR. Although these four muscles are active at a low level during the presentation of the rotating stimulus, when the WSA increased, they are most strongly correlated with the slow decrease in WSA following the transient increase in WSA at stimulus onset. Therefore, the muscles that were strongly recruited during trials in bin1 were ones known to be active during decreases in WSA.

For the inside wing, the activity of several muscles varied linearly with WSA, again suggesting that flies use several muscles to regulate the sustained decreases in WSA during the PSR (Figure 3.4C). The mean activities of b1, iii2, iii3, and i2, were significantly different across the data bins, indicating that these muscles, particularly iii3, and i2, are important in the modulating the gradual and sustained decreases in WSA. These four muscles are all tonic and known to be correlated with WSA. Conversely, the mean activities of iv2, and iv3 for the different bins do not show any difference, suggesting minor involvement of these muscles. Overall, these results suggest that several muscles contribute to regulating WSA during the presentation of the rotating stimulus and during the PSR.

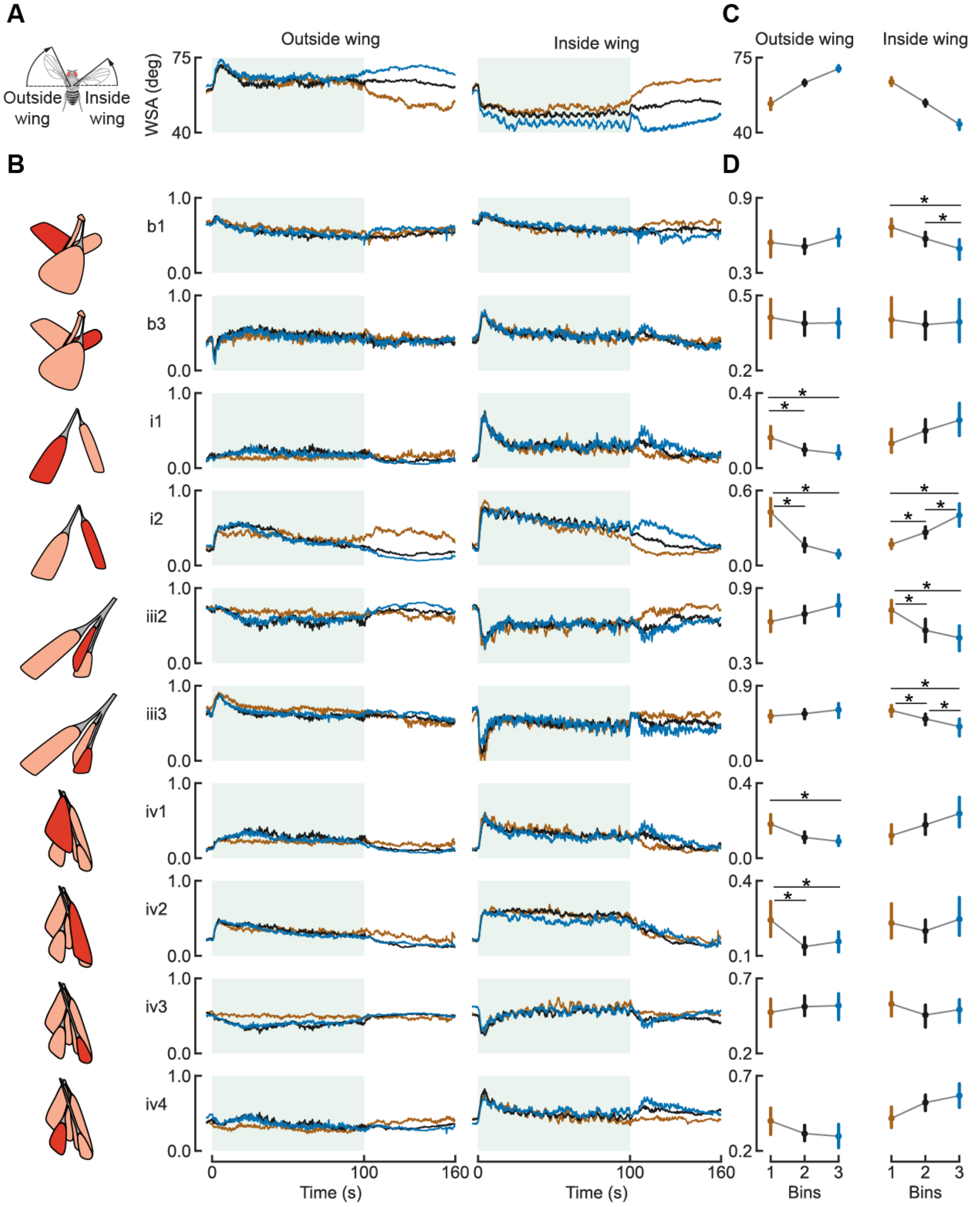

Figure 3.4: Steering muscle activity during the presentation of a rotating scene, and the subsequent PSR.

(A) On the left: Schematic of the turning response of a fly showing the outside wing, which increases in WSA, and the inside wing, which decreases in WSA in response to a scene moving to the right. On the right: Mean WSA traces corresponding to the three data bins. Bin 1 (34 trials) is shown in brown, bin 2 in black (64 trials), and bin 3 in blue (34 trials). The green patch indicates the duration of the rotating scene. The white background indicates presentation of a static scene.

(B) On the left: Schematic of the steering muscles attached to each sclerite, with the relevant muscle shown in red. On the right: Mean muscle activity traces corresponding to the three data bins. Bin 1 is shown in brown, bin 2 in black, and bin 3 in blue. The green patch indicates the duration of the rotating scene. The white background indicates presentation of a static scene.

(C) The dots show the mean WSA of each data bins during the PSR, and the vertical lines the 95% CI across trials in that bin.

(D) The dots show the mean muscle activity of each data bins during the PSR, and the vertical lines the 95% CI across trials in that bin. To determine if the mean muscle activity of each data bin is significantly different from the other two, I performed a permutation test using 10000 permutation replicates and indicated significant differences (p<0.005) between the mean of each bin with an asterisk.

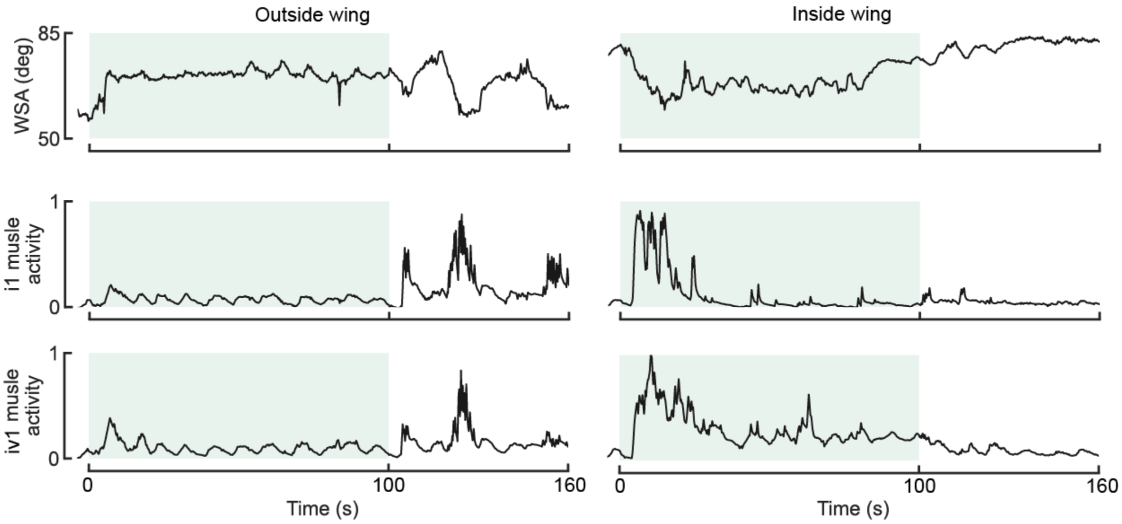

Figure 3.5: Example traces of WSA and corresponding muscle activity traces of i1 and iv1 showing the activity of both muscles occurs mostly in bursts.

As shown in this example, the activity of these muscles is strongly correlated, consistent with previous literature (Melis et al., 2024).

The WSA during the PSR is predicted by the activity of multiple steering muscles

A previous study (Lindsay et al., 2017) found that the scaled sum of muscle activity, particularly from muscles iii3 and i2, can predict WSA with reasonable accuracy. This is consistent with my results thus far showing that these two tonic muscles exhibit a graded response correlated with WSA during the PSR. To build on this result and determine which muscles can best predict the WSA traces during the PSR, I first regressed each muscle signal individually against the WSA for all trials (Figure 3.6A). I then repeated the procedure using all 4083 possible combinations of muscles. To evaluate the goodness of fit for each of these combinations, I calculated the variance explained by each linear model.

The variance explained using individual muscle signals in the linear model (Figure 3.6B) reveals that the activity of muscle iii3, most accurately predicts the WSA for the outside wing. For the inside wing, the activity of i2, provides the best prediction. The activity of iv4 also significantly predicts WSA for both the inside and outside wings. It is important to note that the activity of iii3 shows a positive correlation with WSA, while the activity of i2 and iv4 shows a negative one (the correlations of muscle activity with WSA are explicitly analyzed in the next section). All the muscles that are highly predictive of WSA during the PSR were previously classified as tonic muscles, which is consistent with maintaining wing kinematics over a prolonged duration. The addition of more muscle signals to the linear model resulted in a better prediction of WSA (Figure 3.6C). This is consistent with the values of variance explained obtained using the activities of individual muscles. While iii3, i2, and iv4 are the most predictive, their variance explained is not that much higher than the ones obtained for the rest of the steering muscles. Altogether, these results show that the activity of multiple steering muscles, across different anatomical classes are involved in the regulation of the sustained steering response after OMR stimulation. It is important to note that the values of variance explained using the activity of individual muscles (Figure 3.6B) do not add up to one, because the activity of many the steering muscles is strongly correlated. For example, the activity of iii3 and iii2 are strongly correlated to each other, as is the activity of i2, i1, and iv1. Recent work (Melis et al., 2024) has described in detail how the steering muscles work together to exert tension on each sclerite and so it is expected that many of these muscles exhibit similar patterns of activity.

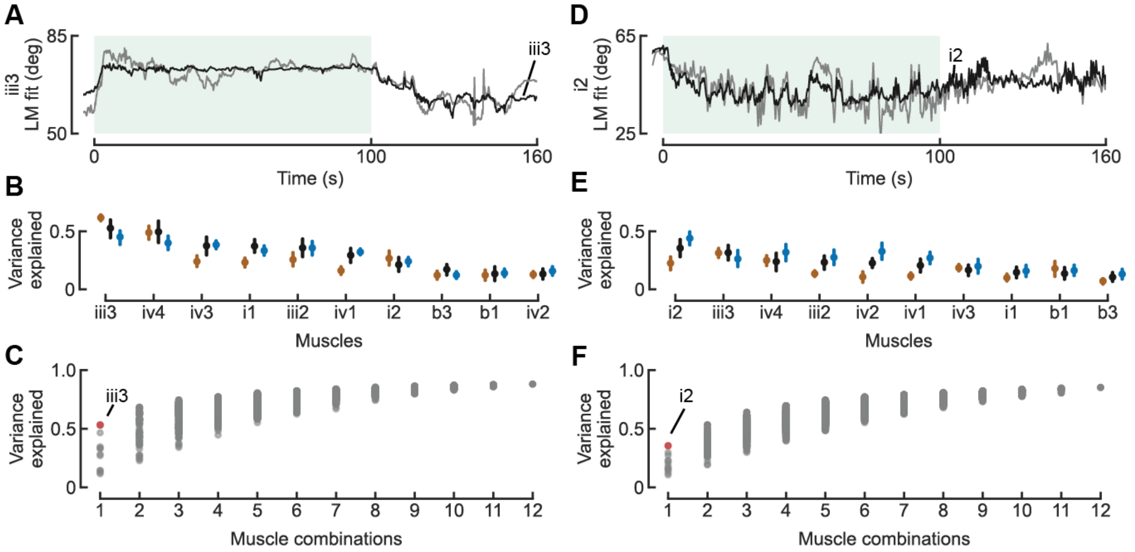

Figure 3.6: The activity of multiple steering muscles predicts the WSA during the PSR.

(A) Example trace of the WSA for the outside wing (gray), and the linear model fit constructed from the activity of the iii3 (black).

(B) The variance explained by the linear model (LM) built using the activity of each muscle. The dots show the mean variance explained of trials in each of the data bins, and the vertical lines the 95% CI. Bin 1 is shown in brown, bin 2 in black, and bin 3 in blue.

(C) The variance explained as a function of the number of muscles used in the model. Each gray dot is the variance explained for every combination of muscle signals.

Correlation of WSA and muscle activity during the OMR stimulation and PSR

I analyzed the relationship between each muscle and WSA during both the rotating stimulus presentation and the subsequent static pattern presentation during which the PSR was measured. I pooled data from all the trials and individuals and plotted the 2D kernel density estimate of muscle activity and WSA. I then fit a linear model for the muscle activity and WSA using the RANSAC algorithm (Figure 3.7). The slopes of the linear fits are listed in Table 3.1. When comparing the correlations between the outside and inside wing, it is important to note that because one wing is increasing in WSA while the other one decreases, the amplitudes sampled are not the same. For the outside wing, the amplitudes range *roughly* between 60 and 75 deg; for the inside wing, the amplitudes range between 35 and 60 deg. For most of the muscles, the slopes of the correlations during the OMR stimulation and during the subsequent PSR do not change sign. This suggests that the regulation of WSA during the presentation of visual motion occurs in the same fashion as during the PSR.

The correlations between muscle activity and WSA are consistent with my previous analysis and broadly consistent with the existing literature (Lindsay et al., 2017; Melis et al., 2024). For example, the activity of b3, i1, i2, are negatively correlated with WSA, whereas the activity of iii2, iii3 are strongly positively correlated with WSA. However, the reported correlations between WSA and the activity of the iv3 and iv4 muscles varies across studies. For example, Lindsay and coworkers (Lindsay et al., 2017) found the activity of iv3 and to be iv4 to be negatively correlated with WSA, while Melis and coworkers (Melis et al., 2024) found a positive correlation between WSA and the activity of iv3 and iv4. In my analysis, I found the activity of iv3 to be positively correlated with WSA, and the activity of iv4 negatively correlated with WSA. These differences may come from the different experimental conditions used across the different experiments. For example, the arena used here and, in the Lindsay et al., 2017 study only measures WSA, while Melis and coworkers measured all three wing kinematic angles. Also, the behavioral repertoire measured is different across studies, Melis and coworkers focused on short flight sequences (~3 s), while I measured muscle activity during long flight bouts.

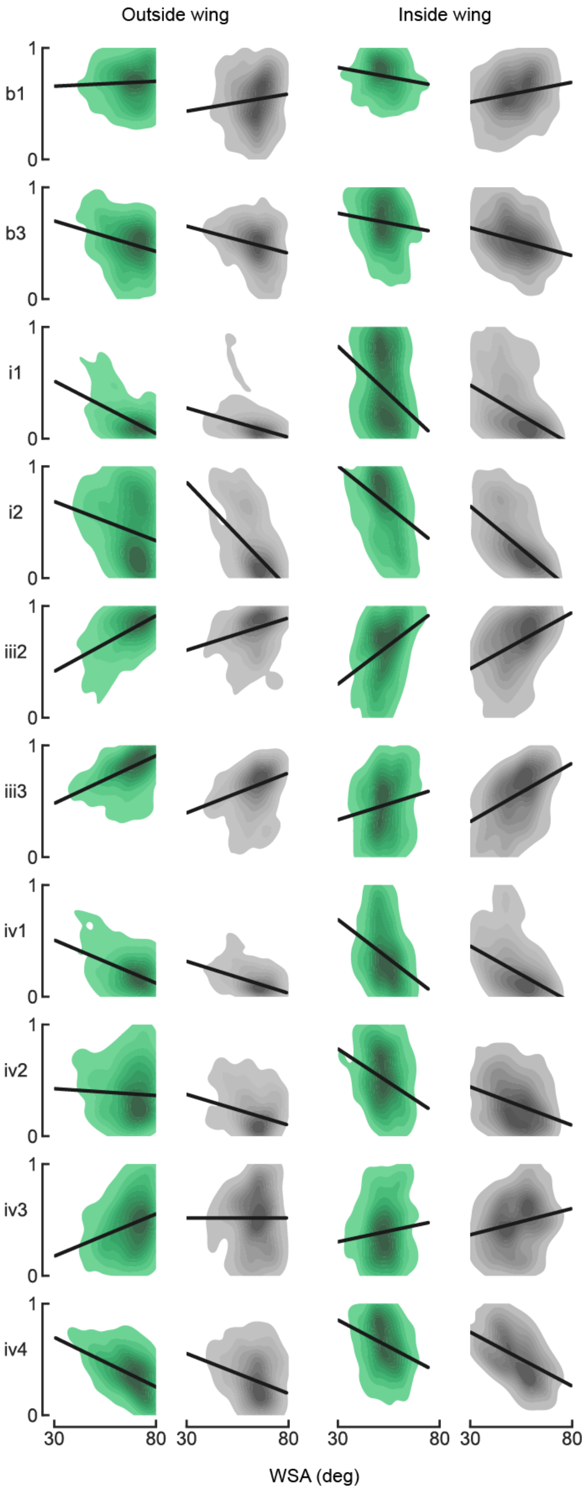
Outside wing
Inside wing
b1
b3
i1
i2
iii2
iii3
iv1
iv2
iv3
iv4
1
0
30
80
WSA (deg)

Figure 3.7: Correlation analysis of muscle activity and WSA.

For the outside wing and inside wing, the first column shows the correlation of the muscle activity and WSA during the presentation of the rotating stimulus plotted as a kernel density estimate in green. The black lines show the fitted linear model. The second column shows the correlations of the muscle activity and WSA during the PSR plotted as a kernel density estimate in gray. The black lines show the fitted linear model.

	Outside wing		**Inside wing**	
Muscle	**Moving scene**	**Static scene**	**Moving scene**	**Static scene**
b1	0.05	0.11	-0.13	0.16
b3	-0.33	-0.23	-0.22	-0.30
i1	-0.55	-0.30	-0.49	-0.55
i2	-0.30	-0.98	-0.64	-0.70
iii2	0.55	0.31	0.46	0.48
iii3	0.41	0.34	0.22	0.50
iv1	-0.40	-0.27	-0.55	-0.51
iv2	-0.03	-0.31	-0.47	-0.29
iv3	0.34	0.02	0.14	0.25
iv4	-0.50	-0.29	-0.38	-0.51

Table 3.1: Slopes of the linear fits between muscle activity and WSA shown in Figure 3.7.

3.4 Discussion

The OMR is understood as a form of trimming the motor system to account for a locomotory bias due to either internal or external perturbations. In this chapter, I examined how the fly's musculature generates the large asymmetric changes in wing motion during the OMR, and focused specifically on which muscles are involved in maintaining the PSR. Previous work (Lindsay et al., 2017; Whitehead et al., 2022) has suggested that the two distinct physiological groups of steering muscles, phasic and tonic, may actuate the integral and proportional control respectively. However, which muscles implement the integral gain during the yaw OMR had not been fully investigated.

Consistent with previous literature (Lindsay et al., 2017), my results show that multiple muscles are involved in the regulation of WSA during the OMR stimulation and found that this is also the case during the PSR (Figure 3.4B). However, the activity of several tonic muscles, such as i2, iii2, iii3, i2, iv1, and iv2 exhibited a graded response correlated with WSA during the PSR (Figure 3.4D). To determine which muscle signals could best predict the WSA traces during the PSR, I regressed the activity of each muscle individually against the WSA traces (Figure 3.6). For the wing that maintained an increase in WSA (outside wing) during the PSR, the activity of muscle iii3 provided the best prediction. This is a tonic muscle whose activity is correlated with increases in stroke amplitude (Figure 3.7). Conversely, for the wing that exhibited a decrease in amplitude during the PSR (inside wing), the activity of muscle i2 most accurately predicted the WSA. This is also a tonic muscle, but its activity is negatively correlated with WSA (Figure 3.7).

Overall, my results show that the regulation of WSA during the OMR stimulation, and subsequent PSR, depends on the activity of multiple muscles. Thus, the implementation of the integral gain of the OMR, is likely distributed among the fly's steering muscle system, particularly the tonic muscles iii3 and i2.

3.5 Materials and methods

Experimental subject details and preparation

All experiments were conducted on 4-5 day old female flies reared at 25ºC on a 12:12 hour light-dark cycle, and fed with standard corn meal fly food supplemented with yeast. I generated flies expressing GCaMP7f in all steering muscles in an HCS wild-type background by crossing HCS, GCaMP7f/Cyo, 22H05-Gal4/Tm6B flies to HCS wild-type flies. Flies were immobilized on a 4ºC cold plate and tethered to a 0.13 mm diameter tungsten wire using UV-activated glue (Henkel; Bondic Inc.). I fixed the head of each fly to its thorax by applying an additional drop of glue of their neck and removed the two front legs at the coxa to allow a clear view of all steering muscles during imaging. All flies were allowed to recover tethered to the pin for at least 30 min before being tested.

Muscle imaging arena

For the muscle imaging experiments, I used a rigid tether flight arena equipped with epifluorescent optics that allow for imaging of all the steering muscles through the flies' cuticle using a previously described technique (Lindsay et al., 2017). There are two muscle imaging setups, one on each side of the arena, to simultaneously image the left and right wing steering muscles while tracking the fly's WSA. Each imaging setup consisted of a blue LED (M470L3, Thor Labs) used as an excitation light source, which was directed through a 480/40 nm filter and focused onto the fly using a 10x lens (CFI Plan Fluor, Nikon). The resulting GCaMP7f fluorescence was collected through a 535/50 nm emission filter (Chroma) and captured by a machine vision camera (BFS-U3-16S2M-CS, FLIR). I used a wingbeat analyzer to monitor the precise timing of single strokes and frequency. This timing signal was used to strobe the blue excitation LED for 1 ms at the dorsal stroke reversal of each wingbeat. The camera was strobed at half the wingbeat frequency (~100 fps), resulting in each frame containing two consecutive illuminations of the thorax. The phase of the epiillumination light was restricted in this manner to reduce motion blur and ensure that light was not delivered to the fly while the wing was obscuring the thorax during the down stroke.

For wing tracking, I used an IR light source (850 nm, Thorlabs Inc. #M850L3) to illuminate the fly, and captured images at 30 fps using a digital camera (BFS-U3-16S2M-CS, FLIR) equipped with a macro lens (MLM3X-MP, Computar) and IR-pass filter (B-46RM72-GB, Hoya) to exclude extraneous light from the LED display. I presented visual stimuli using a circular (12 x 4 panels, 96 x 36 pixels) arena constructed with blue LED (470 nm) panels that spanned 120° around the fly's azimuth, and 60° in elevation from the fly's horizon. To track the wing stroke amplitude during flight, I used Kinefly, a previously described real-time machine-vision system (Suver et al., 2016). The visual patterns used during all periods were starfield patterns, which are described in Lindsay et al, 2017.

Unmixing of the muscle signals

To obtain unmixed traces from the images, I used a previously described method (Lindsay et al., 2017) with minor modifications. The code used for the analysis is publicly available (https://github.com/willdickson/find_fly_angle).

Quantification and statistical analyses

Behavioral data were analyzed with custom software written in Python. Sample sizes refer to the number of individuals tested. Variance across individuals was quantified as the bootstrapped 95% confidence interval (CI), with 1000 bootstrapped iterations for the mean of the individual means.

References

Dickinson, M. (2006). Insect flight. *Current Biology* **16**, R309–R314.

Heide, G. (1983). Neural mechanisms of flight control in Diptera. *In W. Nachtigall (ed)* **BIONA-report**, pp 35-52.

Josephson, R. K., Malamud, J. G. and Stokes, D. R. (2000). Asynchronous Muscle: A Primer. *Journal of Experimental Biology* **203**, 2713–2722.

Lindsay, T., Sustar, A. and Dickinson, M. (2017). The Function and Organization of the Motor System Controlling Flight Maneuvers in Flies. *Current Biology* **27**, 345–358.

Melis, J. M., Siwanowicz, I. and Dickinson, M. H. (2024). Machine learning reveals the control mechanics of an insect wing hinge. *Nature* **628**, 795–803.

O'Sullivan, A., Lindsay, T., Prudnikova, A., Erdi, B., Dickinson, M. and Philipsborn, A. C. von (2018). Multifunctional Wing Motor Control of Song and Flight. *Current Biology* **28**, 2705-2717.e4.

Pringle, J. W. S. (1949). The excitation and contraction of the flight muscles of insects. *The Journal of Physiology* **108**, 226–232.

Pringle, J. W. S. (1957). *Insect Flight*. Cambridge University Press.

Schnell, B., Weir, P. T., Roth, E., Fairhall, A. L. and Dickinson, M. H. (2014). Cellular mechanisms for integral feedback in visually guided behavior. *Proceedings of the National Academy of Sciences* **111**, 5700–5705.

Suver, M. P., Huda, A., Iwasaki, N., Safarik, S. and Dickinson, M. H. (2016). An Array of Descending Visual Interneurons Encoding Self-Motion in Drosophila. *J Neurosci* **36**, 11768–11780.

Tammero, L. F. and Dickinson, M. H. (2002). Collision-avoidance and landing responses are mediated by separate pathways in the fruit fly, Drosophila melanogaster. *Journal of Experimental Biology* **205**, 2785–2798.

Tammero, L. F., Frye, M. A. and Dickinson, M. H. (2004). Spatial organization of visuomotor reflexes in Drosophila. *Journal of Experimental Biology* **207**, 113–122.

Trimarchi, J. R. and Schneiderman, A. M. (1994). The motor neurons innervating the direct flight muscles of Drosophila melanogaster are morphologically specialized. *J Comp Neurol* **340**, 427–443.

Tu, M. S. and Dickinson, M. H. (1994). Modulation of Negative Work Output from a Steering Muscle of the Blowfly Calliphora Vicina. *Journal of Experimental Biology* **192**, 207–224.

Whitehead, S. C., Leone, S., Lindsay, T., Meiselman, M. R., Cowan, N. J., Dickinson, M. H., Yapici, N., Stern, D. L., Shirangi, T. and Cohen, I. (2022). Neuromuscular embodiment of feedback control elements in Drosophila flight. *Science Advances* **8**, eabo7461.

Chapter 4

CONCLUSIONS

Flying insects, such as the fruit fly *Drosophila melanogaster*, are capable of traveling large distances in a variety of environmental conditions while maintaining a straight trajectory (Coyne et al., 1982; Götz, 1987; Leitch et al., 2021). To travel such distances, they must rely on some form of navigation to maintain a constant heading over time. In addition, they must constantly integrate sensory information to adjust for external and internal perturbations to ensure they maintain stable flight along their desired trajectory. Previous studies have shown that flies can maintain a constant groundspeed despite varying wind conditions (David, 1978; Leitch et al., 2021), perform quick turns to evade predators (Srinivasan and Zhang, 2004), and even sustain flight despite having extensive wing damage (Muijres et al., 2017; Salem et al., 2022).

In this thesis, I focus on behavioral algorithms flies rely on to maintain a straight and stable trajectory. In Chapter 1, I describe the results of field experiments I took part in to uncover the strategies flies use when dispersing large distances (Leitch et al., 2021). Using a series of release-and-recapture experiments performed under different wind conditions, we found that flies can, to some extent regulate their groundspeed in a variety of wind conditions, and are not simply advected by the wind. We also proposed an agent-based model in which animals maintain a fixed body orientation relative to celestial cues (Giraldo et al., 2018; Weir and Dickinson, 2012), actively regulate groundspeed along their body axis, and allow the wind to advect them sideways.

In Chapter 2, I focus on characterizing the controller underlying the optomotor response (OMR), a flight stabilization behavior. The OMR is understood as a form of trimming the motor system to account for a locomotory bias due to either internal or external perturbations

(Götz, 1968). I used a combination of experimental and control theory approaches to determine that the fly's behavior during the OMR is best approximated by a proportional-integral controller (PI). While previous studies had noted the integrative characteristics of the OMR, the size and possible effect of the integral gain had not been fully characterized. By using a simulation, I then explored the potential implications of an integral gain in the fly's natural flight behaviors. It is important to note that the phenomenology I describe in Chapter 2 has also been observed in locusts (Möhl, 1988), suggesting that an integrative element of the OMR is present across different insect species. While all my experimental data is consistent with an integrative element in the feedback control loop of the OMR, more work is needed to determine if this integral gain is used in naturalist flight behaviors.

To examine how the fly's motor system might implement this control strategy, in Chapter 3, I measured the activity of the steering muscles in a behaving fly. I found that multiple steering muscles are likely involved in the implementation of the integral gain. Recent electron microscopy datasets and connectome analyses for the adult fly brain (Scheffer et al., 2020; Zheng et al., 2018) and ventral nerve cord (Phelps et al., 2021; Takemura et al., 2023) provide the opportunity for future studies to examine the neural circuits implementing the PI feedback control. Thus, this study provides an entry point to identify descending neurons that innervate the tonic muscles most relevant to the implementation of the integral gain. While the neural circuits involved in the processing of visual signals have been identified, neurons that regulate the motion of the wings and some other body parts during the OMR remain to be fully characterized (Ryu et al., 2022). Identifying the neural circuits involved in the PI control of the OMR constitutes a significant effort, which is outside the scope of the current study. However, the outcomes of which could have profound impacts on our understanding of how neural circuits implement feedback control.

References

Coyne, J. A., Boussy, I. A., Prout, T., Bryant, S. H., Jones, J. S. and Moore, J. A. (1982). Long-Distance Migration of Drosophila. *The American Naturalist* **119**, 589–595.

David, C. T. (1978). The relationship between body angle and flight speed in free-flying Drosophila. *Physiological Entomology* **3**, 191–195.

Giraldo, Y. M., Leitch, K. J., Ros, I. G., Warren, T. L., Weir, P. T. and Dickinson, M. H. (2018). Sun Navigation Requires Compass Neurons in Drosophila. *Current Biology* **28**, 2845-2852.e4.

Götz, K. G. (1968). Flight control in Drosophila by visual perception of motion. *Kybernetik* **4**, 199–208.

Götz, K. G. (1987). Course-Control, Metabolism and Wing Interference During Ultralong Tethered Flight in Drosophila Melanogaster. *Journal of Experimental Biology* **128**, 35–46.

Leitch, K. J., Ponce, F. V., Dickson, W. B., van Breugel, F. and Dickinson, M. H. (2021). The long-distance flight behavior of Drosophila supports an agent-based model for wind-assisted dispersal in insects. *Proceedings of the National Academy of Sciences* **118**, e2013342118.

Möhl, B. (1988). Short-term learning during flight control inLocusta migratoria. *J. Comp. Physiol.* **163**, 803–812.

Muijres, F. T., Iwasaki, N. A., Elzinga, M. J., Melis, J. M. and Dickinson, M. H. (2017). Flies compensate for unilateral wing damage through modular adjustments of wing and body kinematics. *Interface Focus* **7**, 20160103.

Phelps, J. S., Hildebrand, D. G. C., Graham, B. J., Kuan, A. T., Thomas, L. A., Nguyen, T. M., Buhmann, J., Azevedo, A. W., Sustar, A., Agrawal, S., et al. (2021). Reconstruction of motor control circuits in adult Drosophila using automated transmission electron microscopy. *Cell* **184**, 759-774.e18.

Ryu, L., Kim, S. Y. and Kim, A. J. (2022). From Photons to Behaviors: Neural Implementations of Visual Behaviors in Drosophila. *Front. Neurosci.* **16**,.

Salem, W., Cellini, B., Kabutz, H., Hari Prasad, H. K., Cheng, B., Jayaram, K. and Mongeau, J.-M. (2022). Flies trade off stability and performance via adaptive compensation to wing damage. *Science Advances* **8**, eabo0719.

Scheffer, L. K., Xu, C. S., Januszewski, M., Lu, Z., Takemura, S., Hayworth, K. J., Huang, G. B., Shinomiya, K., Maitlin-Shepard, J., Berg, S., et al. (2020). A connectome and analysis of the adult Drosophila central brain. *eLife* **9**, e57443.

Srinivasan, M. V. and Zhang, S. (2004). Visual motor computations in insects. *Annu Rev Neurosci* **27**, 679–696.

Takemura, S., Hayworth, K. J., Huang, G. B., Januszewski, M., Lu, Z., Marin, E. C., Preibisch, S., Xu, C. S., Bogovic, J., Champion, A. S., et al. (2023). A Connectome of the Male Drosophila Ventral Nerve Cord. 2023.06.05.543757.

Weir, P. T. and Dickinson, M. H. (2012). Flying *Drosophila* Orient to Sky Polarization. *Current Biology* **22**, 21–27.

Zheng, Z., Lauritzen, J. S., Perlman, E., Robinson, C. G., Nichols, M., Milkie, D., Torrens, O., Price, J., Fisher, C. B., Sharifi, N., et al. (2018). A Complete Electron Microscopy Volume of the Brain of Adult Drosophila melanogaster. *Cell* **174**, 730-743.e22.